SOUTHERN PLAINS
TRANSPORTATION CENTER

Development of a Mechanistic-based Design Method for Geosynthetic-Reinforced Pavement on Expansive Soils and Prediction of Moisture Content Fluctuations in Subgrades

Jay X. Wang, Ph.D., P.E.
Debojit Sarker, Ph.D. Student
Berjees Ikra, M.S.

SPTC15.1-23-F

Southern Plains Transportation Center
201 Stephenson Parkway, Suite 4200
The University of Oklahoma
Norman, Oklahoma 73019

DISCLAIMER

The contents of this report reflect the views of the authors, who are responsible for the facts and accuracy of the information presented herein. This document is disseminated under the sponsorship of the Department of Transportation University Transportation Centers Program, in the interest of information exchange. The U.S. Government assumes no liability for the contents or use thereof.

TECHNICAL REPORT DOCUMENTATION PAGE

1. REPORT NO.	2. GOVERNMENT ACCESSION NO.	3. RECIPIENTS CATALOG NO.
SPTC15.1-23-F		

4. TITLE AND SUBTITLE	5. REPORT DATE
Development of a Mechanistic-based Design Method for Geosynthetic-Reinforced Pavement on Expansive Soils and Prediction of Moisture Content Fluctuations in Subgrades	October 5, 2018
	6. PERFORMING ORGANIZATION CODE
7. AUTHOR(S) Jay X. Wang, Ph.D., P.E., Debojit Sarker, Ph.D student, Berjees Ikra, M.S.	8. PERFORMING ORGANIZATION REPORT
9. PERFORMING ORGANIZATION NAME AND ADDRESS Programs of Civil Engineering and Construction Engineering Technology Louisiana Tech University 600 Dan Reneau Dr., Ruston, LA 71272	10. WORK UNIT NO.
	11. CONTRACT OR GRANT NO. DTRT13-G-UTC36
12. SPONSORING AGENCY NAME AND ADDRESS Southern Plains Transportation Center 201 Stephenson Pkwy, Suite 4200 The University of Oklahoma Norman, OK 73019	13. TYPE OF REPORT AND PERIOD COVERED Final April 2017 – June 2018
	14. SPONSORING AGENCY CODE

15. SUPPLEMENTARY NOTES
University Transportation Center

16. ABSTRACT
A methodology has been developed to compute bending moments and shear forces, etc., in geosynthetic-reinforced pavement on expansive soils. The geosynthetic-reinforced pavement, subjected to the heave/shrinkage-induced vertical displacement caused by the volume change of expansive subgrade soils, was formulated using the Timoshenko beam theory. The virtual load method (VLM) was developed by applying a virtual load on the pavement to make the beam deflection equivalent to the heave/shrinkage-induced vertical displacement. The unknown virtual load was expressed as a Fourier series, and the Fourier constants were determined by employing the inverse theory for the identification of material parameters. As a case study, the virtual load method was applied to investigate the effect of geosynthetics on the research road FM 2 near the city of College Station in Texas, USA. The geosynthetics in the pavement functioned as a reinforcement to reduce the pavement damage caused by the seasonal swell and shrinkage of the expansive subgrade soils. This research may help develop a proper and implementable design and construction method to mitigate the harmful effect of expansive clays on highway pavements. Additionally, numerical prediction was performed for the moisture content fluctuation in expansive subgrade clay due to climate changes. It was completed using commercial software VADOSE/W in analyzing the changes in moisture content over a one-year period. Moisture content fluctuations from the numerical analyses were validated by the long-term moisture content measurements below the pavement of country road FM 2. The research achievements have shown that multiple weather conditions can be considered and integrated while predicting the moisture content fluctuations, which could lead to more accurate heave/shrinkage predictions.

17. KEY WORDS	18. DISTRIBUTION STATEMENT
Virtual Load Method, Closed-form solution, Timoshenko Beam, Pasternak Foundation, Pavement, Moisture Content Fluctuation Prediction, Expansive soil, Louisiana.	No restrictions. This publication is available at www.sptc.org and from the NTIS.

19. SECURITY CLASSIF. (OF THIS REPORT)	20. SECURITY CLASSIF. (OF THIS PAGE)	21. NO. OF PAGES	22. PRICE
Unclassified	Unclassified	72 + cover	

SI* (MODERN METRIC) CONVERSION FACTORS				
APPROXIMATE CONVERSIONS TO SI UNITS				
SYMBOL	**WHEN YOU KNOW**	**MULTIPLY BY**	**TO FIND**	**SYMBOL**
		LENGTH		
in	inches	25.4	millimeters	mm
ft	feet	0.305	meters	m
vd	vards	0.914	meters	m
mi	miles	1.61	kilometers	km
		AREA		
in^2	square inches	645.2	square millimeters	mm^2
ft^2	square feet	0.093	square meters	m^2
vd^2	square yard	0.836	square meters	m^2
ac	acres	0.405	hectares	ha
mi^2	square miles	2.59	square kilometers	km^2
		VOLUME		
fl	fluid ounces	29.57	milliliters	mL
oz	gallons	3.785	liters	L
gal	cubic feet	0.028	cubic meters	m^3
		MASS		
oz	ounces	28.35	grams	g
lb	pounds	0.454	kilograms	kg
T	short tons (2000 lb)	0.907	megagrams (or "metric ton")	Mg (or "t")
		TEMPERATURE (exact degrees)		
^oF	Fahrenheit	5 (F-32)/9	Celsius	^oC
		ILLUMINATION		
fc	foot-candles	10.76	lux	lx
fl	foot-Lamberts	3.426	candela/m^2	cd/m^2
		FORCE and PRESSURE or STRESS		
lbf	poundforce	4.45	newtons	N
lbf/in^2	poundforce per square inch	6.89	kilopascals	kPa
APPROXIMATE CONVERSIONS FROM SI UNITS				
SYMBOL	**WHEN YOU KNOW**	**MULTIPLY BY**	**TO FIND**	**SYMBOL**
		LENGTH		
mm	millimeters	0.039	inches	in
m	meters	3.28	feet	ft
m	meters	1.09	vards	vd
km	kilometers	0.621	miles	mi
		AREA		
mm^2	square millimeters	0.0016	square inches	in^2
m^2	square meters	10.764	square feet	ft^2
m^2	square meters	1.195	square yards	vd^2
ha	hectares	2.47	acres	ac
km^2	square kilometers	0.386	square miles	mi^2
		VOLUME		
mL	milliliters	0.034	fluid ounces	fl oz
L	liters	0.264	gallons	gal
m^3	cubic meters	35.314	cubic feet	ft^3
m^3	cubic meters	1.307	cubic yards	vd^3
		MASS		
g	grams	0.035	ounces	oz
kg	kilograms	2.202	pounds	lb
Mg (or "t")	megagrams (or "metric ton")	1.103	short tons (2000 lb)	T
		TEMPERATURE (exact degrees)		
^oC	Celsius	1.8C+32	Fahrenheit	^oF
		ILLUMINATION		
lx	lux	0.0929	foot-candles	fc
cd/m^2	candela/m^2	0.2919	foot-Lamberts	fl
		FORCE and PRESSURE or STRESS		
N	newtons	0.225	poundforce	lbf
kPa	kilopascals	0.145	poundforce per square h	lbf/in^2

*SI is the symbol for the International System of Units. Appropriate rounding should be made to comply with Section 4 of ASTM E380. (Revised March 2003)

ACKNOWLEDGMENTS

The research presented in this report was sponsored by the Southern Plains Transportation Center (SPTC) under contract No. SPTC15.1-23. The authors would like to express their gratitude to Dr. Md. Adnan Khan for his valuable suggestions, Mr. Harold "Skip" Paul of former LTRC director, Mr. Daniel Thompson at Aillet, Fenner, Jolly & McClelland, Mr. Gary Hubbard at Greater Bossier Economic Development Foundation, and Shams Arafat at Louisiana Tech University for their assistances in providing various information.

Development of a Mechanistic-based Design Method for Geosynthetic-Reinforced Pavement on Expansive Soils and Prediction of Moisture Content Fluctuations in Subgrades

Final Report

October 5, 2018

Jay X. Wang, Ph.D., P.E.

Debojit Sarker, Ph.D. Student

Berjees Ikra, M.S.

Southern Plains Transportation Center

201 Stephenson Pkwy, Suite 4200

The University of Oklahoma

Norman, OK 73019

TABLE OF CONTENTS

1. IMPLEMENTABLE MODELING OF GEOSYNTHETIC-REINFORCED PAVEMENT ON EXPANSIVE SOILS 1

1.1 INTRODUCTION 1

1.2 MODELING OF TIMOSHENKO BEAM ON PASTERNAK FOUNDATION 3

1.3 VIRTUAL LOAD METHOD (VLM) TO FIND A CLOSED-FORM SOLUTION OF PAVEMENT ON EXPANSIVE SOILS 6

1.3.1 The forward analysis of geosynthetic-reinforced pavement on elastic foundation 7

1.3.2 Beam deflection $W_B(x)$ due to load q 8

1.3.3 Pavement rotation $\Phi(x)$ due to q load 10

1.3.4 Pavement moment M(x) due to q load 12

1.3.5 Pavement shear Q(x) due to q load 13

1.3.6 Boundary conditions 16

1.3.7 The inverse analysis of geo-synthetic reinforced pavement on expansive soils 18

2. THE REINFORCEMENT EFFECT OF GEOSYNTHETICS ON THE PAVEMENT OF RESEARCH ROAD FM 2, TX, USA 20

2.1 VERTICAL DEFORMATION OF THE SUBGRADE EXPANSIVE SOIL 21

2.2 MATERIAL PROPERTIES OF THE PAVEMENT-FOUNDATION SYSTEM 21

2.3 ANALYSIS OF GEOSYNTHETIC-REINFORCED PAVEMENT DUE TO EXTREME SOIL HEAVE/SHRINKAGE CONDITION 23

3. NUMERICAL PREDICTION OF MOISTURE FLUCTUATIONS IN UNSATURATED EXPANSIVE CLAY AND HEAVE ANALYSIS UNDER EXTREME WEATHER CONDITIONS 31

3.1 INTRODUCTION 31

3.2 SITE DESCRIPTION OF THE FM 2 PROJECT AND THE FIELD INVESTIGATION 36
3.3 THE VADOSE/W MODEL SETUP 37
3.4 NUMERICAL VALIDATION WITH THE FIELD INVESTIGATION 41
3.4.1 Station 184 41
3.4.2 Station 199 43
3.4.3 Station 84 44
3.5 HEAVE/SHRINKAGE-INDUCED DEFORMATION OF THE SUBGRADE SOIL 46
4. SUMMARY 53
5. REFERENCES 55

LIST OF FIGURES

Figure 1. Swell/Shrinkage Induced Longitudinal Cracks on Pavement Resting on Expansive Soils. 3
Figure 2. Schematic Diagram of 1-D Loaded Beam Supported on Elastic Foundation Model. 4
Figure 3. Sign convention for Deflection, Shear Force, Bending Moment, and Tension (Positive as shown). 5
Figure 4. (a) Pavement on a Regular Soil, (b) Pavement Deflection Due to External Load, (c) Pavement Deflection Due to Expansive Soil's Volume Change, and (d) Proposed Virtual Load Soil Model (Adapted from Khan 2017). 7
Figure 5. Location and layout of FM 2 relative to major metropolitan areas in Texas. .. 20
Figure 6 A schematic diagram of a typical geosynthetic-reinforced pavement on expansive soil. 22
Figure 7. (a) Deflection, (b) virtual load, (c) rotation, (d) shear, (e) bending moment and (f) tension force diagrams for extreme heave condition. 26
Figure 8. (a) Deflection, (b) virtual load, (c) rotation, (d) shear, (e) bending moment and (f) tension force diagrams for extreme shrinkage condition. 27
Figure 9. Constitutive tension surface for geosynthetic-reinforcement (Extreme heave). 29
Figure 10. Constitutive tension surface for geosynthetic-reinforcement (Extreme shrinkage). 29
Figure 11. (a) Location of FM 2 relative to Austin and Houston (b) Layout of FM 2 (Zornberg et al., 2008). 36
Figure 12. Sensor distributions: (a) Horizontal array at Station 84 (b) Vertical array at Stations 184 and 199 (Zornberg et al., 2008). 37
Figure 13. Soil profile with materials and boundary conditions. 38
Figure 14. a) The SWCC used in VADOSE/W model, b) The HCF used in VADOSE/W model (Ikra 2017). 39
Figure 15. Precipitation data over a one-year duration. 40
Figure 16. Temperature data (maximum and minimum) over a one-year duration. 40
Figure 17. Relative humidity data (maximum and minimum) over a one-year duration. 41

Figure 18. (a) Isochrones of measured gravimetric water content data for station 184 (Gupta, 2009), (b) Isochrones of simulated gravimetric water content data for station 184. 42
Figure 19. (a) Time series of measured gravimetric water content data below the ditch for Station 184 (Gupta, 2009), (b) Time series of simulated gravimetric water content data below the ditch for Station 184. 42
Figure 20. (a) Isochrones of measured gravimetric water content data below ditch (Station 199) (Gupta, 2009), (b) Isochrones of simulated gravimetric water content data below ditch (Station 199). 43
Figure 21. (a) Time series of measured gravimetric water content data below ditch (Station 199) (Gupta, 2009), (b) Time series of simulated gravimetric water content data below ditch (Station 199). 44
Figure 22. (a) Isochrones of measured gravimetric water content data for Station 84 - (Gupta 2009), (b) Isochrones of simulated gravimetric water content data for Station 84. 45
Figure 23. (a) Time series of measured gravimetric water content data below pavement (Station 84) (Gupta, 2009), (b) Time series of simulated gravimetric water content data below pavement (Station 84). 45
Figure 24. Sections for heave analysis. 46
Figure 25. Moisture fluctuations with depth (a) section 1 (below pavement center), (b) section 2 (pavement edge) and (c) section 3 (ditch center). 47

LIST OF TABLES

Table 1 Material properties of the pavement-foundation framework 22
Table 2 Maximum and minimum rotation, shear, and moment on pavement and tension in geosynthetics for Texas FM 2 research road by applying the VLM 24
Table 3 Tensile force and virtual load variation of Texas FM 2 road with and without geosynthetics. 28
Table 4 Shrinkage deformation calculation for section 1 from the measured and calculated water content using the Richard and Dhowian equations, respectively..... 48
Table 5 Shrinkage deformation calculation for section 2 from the measured and calculated water content using the Richard and Dhowian equations, respectively..... 49
Table 6 Shrinkage deformation calculation for measured and calculated water content change from the Richard and Dhowian equations for section 3. 50
Table 7 Heave deformation calculation for measured and calculated water content change from the Richard and Dhowian equations for section 3. 51

EXECUTIVE SUMMARY

In the SPTC-funded research project, a methodology has been developed to compute bending moments and shear forces, etc., in geosynthetic-reinforced pavement on expansive soils. The geosynthetic-reinforced pavement, subjected to the heave/shrinkage-induced vertical displacement caused by the volume change of expansive subgrade soils, was formulated by following the Timoshenko beam theory. The virtual load method (VLM) was developed by applying a virtual load on the pavement to make the beam deflection equivalent to the heave/shrinkage-induced vertical displacement. The unknown virtual load was expressed as a Fourier series, and the Fourier constants were determined by employing the inverse theory for the identification of material parameters. A rigorous analytical solution for evaluating the shear force, bending moment etc. acting on geosynthetic reinforced pavement resting over expansive soil was developed. As a case study, the virtual load method was applied to investigate the effect of geosynthetics on the research road FM 2 near the city of College Station in Texas, USA, which was conducted by TxDOT. Parametric studies have shown that geosynthetics without shear stiffness (e.g. geotextile) resist less shear force or bending moment than geosynthetics with shear stiffness (e.g. geogrid) do. The analysis of tension force variations due to the changes in tension modulus can assist pavement designers and industry select size and type of geosynthetics to reinforce pavements overlying expansive subgrade soils to reduce the damages caused by seasonal swelling and shrinkage of the expansive soils. Research achievements have shown that the methodology was successfully applied to analyze the real engineering project. It can be used as a simple and reliable method for pavement design.

Numerical prediction was investigated as well for moisture content fluctuation in expansive subgrade clay due to climate changes and its effect on the pavement sitting on expansive soils. The research was done using commercial software VADOSE/W in analyzing the changes in moisture content over a one-year period of time. The numerical analyses were validated by the long-term moisture content measurements obtained from below the pavement of country road FM 2. The computed moisture content fluctuations were employed for the prediction of the heave/shrinkage-induced deformation of the subgrade soil, which was utilized for the pavement analyses using the above-mentioned analytical model. Multiple weather conditions can be considered and integrated in commercial software VADOSE/W, which could lead to a more accurate prediction of the heave/shrinkage-induced deformations.

1. Implementable Modeling of Geosynthetic-reinforced Pavement on Expansive soils

1.1 Introduction

Volume of expansive clay changes significantly with fluctuation of moisture content. In presence of high moisture content it swells, and during a dry season it shrinks. The large volume change causes severe damage to overlaying light structures. In USA the estimated structural damage due to expansive clay was over $100 billion (Estabragh et al. 2014).

Figure 1. Swell/Shrinkage Induced Longitudinal Cracks on Pavement Resting on Expansive Soils.

shows longitudinal cracks formed in a typical pavement supported by expansive soils. In industry many techniques are used to overcome the adverse effects of expansive clay including compaction, pre-wetting, maintaining constant moisture content, chemical stabilization (Al-Rawas and Goosen 2006; Dang et al. 2016). Chemical stabilization may be a very effective short time solution but under an adverse site condition it shows a poor long-term durability (Chittoori et al. 2011). Moghal et al. (2017) further indicated that chemically stabilized clay performs well under compression, but during summer when the soils are expected to experience tensile force, it underperforms. An efficient solution to this problem is to reinforce the clay. This is done by either including a fiber like material with chemical stabilizer or using geosynthetic products (Jahandari et al. 2017; Kumar et al. 2007; Vessely and Wu 2002; Viswanadham et al. 2009; Yixian et al. 2016; Zornberg 2017).

In this research the structural system of a geosynthetic reinforced pavement resting on expansive soil is investigated. Chenggang (2004) pointed out that the mechanism of reinforcement of geosynthetics is not fully understood, and thereby a significant progress has not been seen in the development of a reliable and accurate

analysis method. Many researchers used various numerical modeling methods to investigate the effects of expansive subgrade on pavements (Cary and Zapata 2014; Djellali et al. 2013; Luo and Prozzi 2010; Siekmeier 2011; Zapata et al. 2009). However, engineering practitioners are still expecting to have a feasible or implementable methodology for the design of pavement structures on expansive soils. It is not a new idea that a pavement was taken as a beam using various beam theories to analyze pavement-soil interaction (Fwa et al. 1996; Ghosh et al. 2017; Musa 2018; Zhao et al. 2016). However, few methods have been developed to consider pavement as a beam on expansive soil by incorporating the deformation of expansive soils in the formulations. Khan and Wang (2017) and Khan (2017) developed a closed-form solution to analyze a reinforcement-free pavement resting on expansive soil. The study presented here is a continuation of the previous research, which has been extended to include the research on the pavement reinforced with geosynthetic, and the interaction is reasonably considered between the geosynthetic materials and expansive subgrade soils. Although the Winkler foundation (one-parameter) is the most popular elastic soil model because of its simplicity, but the Pasternak foundation model (two-parameters) takes into account the effect of shear stiffness with a reasonable accuracy (Ma et al. 2009; Tanahashi 2004; Worku 2014; Yin 2000b; Yu et al. 2017). It might be a model for geosynthetic-reinforced pavement. It is expected that the model would come up with more realistic results. In the research, a series of closed-form solutions have been developed using an inverse analysis, and all the equations and calculations can be incorporated in any programming language. This simplified method will be significantly simple as compared with the conventional numerical models using FEM or FDM, and it can be easily implementable.

It was realized that an inverse problem dealing with the solution of pavement-foundation framework has not been addressed so far. The inverse problems are more difficult and require a suitable blend of a forward method working in conjunction with an appropriate optimization tool (Das 2012). Therefore, in this study, an inverse problem is solved for concurrently evaluating Fourier constants in a pavement foundation framework problem. The pavement deflection is taken as the reference field

corresponding to which the unknowns have been estimated. To demonstrate the estimation precision, the pavement deflection is obtained by initially solving a forward problem with known values of pressure loading. In the inverse method, Linear Least Square method (LLS) (Aster et al. 2013; Golub 1965; Marquardt 1970) is used as a part of conjunction with the forward analysis of the problem. Apart from simple Linear Least Square method (LLS), some other suitable methods e.g. Levenberg-Marquardt method (Levenberg 1944; Marquardt 1963) can also be used.

A rigorous analytical solution was achieved for evaluating the shear force, bending moment etc. acting on geosynthetic-reinforced pavement resting on expansive soil. The pavement embedded within the geosynthetics was simulated as a reinforced Timoshenko beam because it can explicate the deformations of shear and bending concurrently. The underlying expansive soil was simulated by a Pasternak model, which is based on the assumption of pure shearing of the beam.

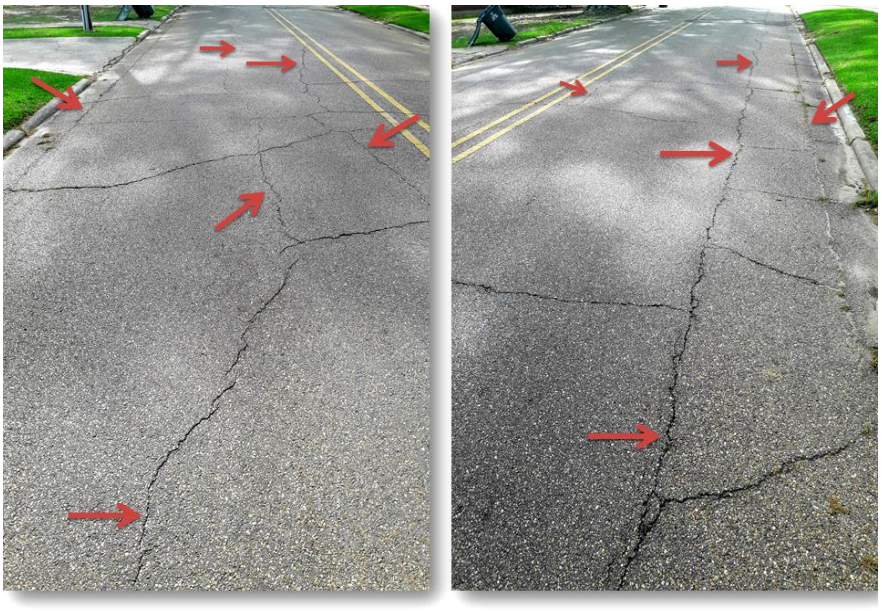

Figure 1. Swell/Shrinkage Induced Longitudinal Cracks on Pavement Resting on Expansive Soils.

1.2 Modeling of Timoshenko beam on Pasternak foundation

In the analytical model, the pavement, which is treated as a beam, was considered symmetric to the central line as shown in **Error! Reference source not found.**. The geosynthetic reinforced pavement was simulated as a reinforced Timoshenko beam. The thickness of the pavement was *h* and both the length of the x-section of the pavement and the length of the geosynthetic reinforcement was *L*. The Pasternak model was used to model the expansive subgrade soil. The Pasternak foundation allows the traverse connection in the supporting subgrade or subbase layer of a pavement to be considered in addition to the subgrade reaction. In this study, the foundation soil was considered as elastic and overlain by a geosynthetic-reinforced pavement. By adopting the Pasternak model, which takes into account the shear resistance of the reinforced pavement, we will be able to consider the effect of geosynthetic reinforcement, and therefore can acquire a deeper understanding of the mechanism of the initiation of and propagation of the pavement cracks due to the heave/shrinkage of expansive subgrade soils.

Error! Reference source not found. shows the reinforcement in a Timoshenko beam resting on an elastic foundation. Two independent variables are, settlement *w* and rotation angle Φ, with the sign convention given in Figure 3. The relationship between moment *M* and the rate of rotation angle change can be expressed (Timoshenko 1921) as

$$M = -D\,\frac{d\Phi}{dx} \tag{1}$$

Where Φ = rotation angle, and *D* is the bending stiffness. The relationship between shear force *Q* and shear deformation γ can be expressed (Timoshenko 1921) as

$$Q = C\gamma = C\left(\frac{dw}{dx} - \Phi\right) \tag{2}$$

Here, *C* is the shear stiffness which will be discussed next.

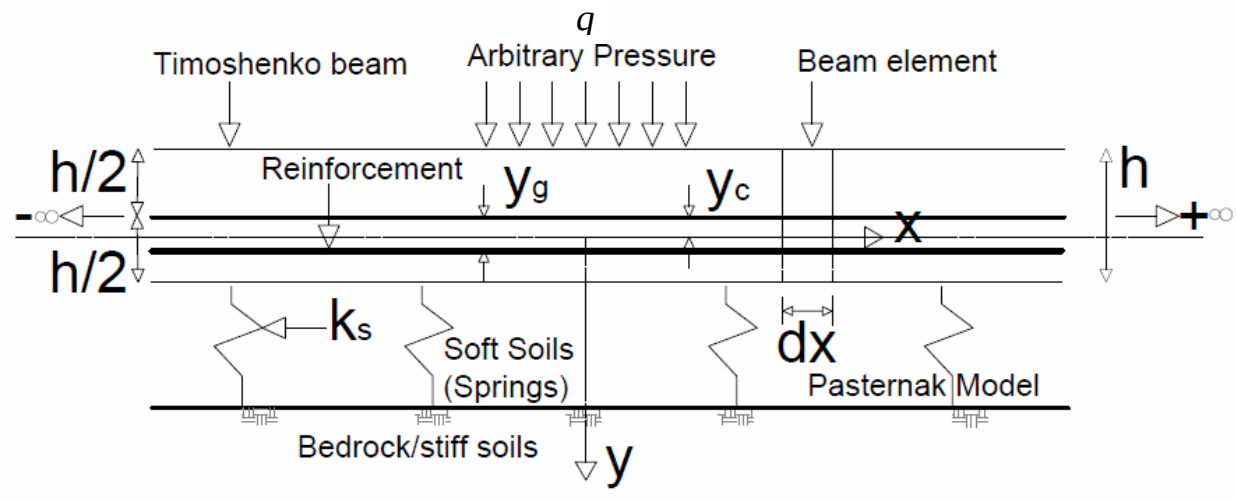

Figure 2. Schematic Diagram of 1-D Loaded Beam Supported on Elastic Foundation Model.

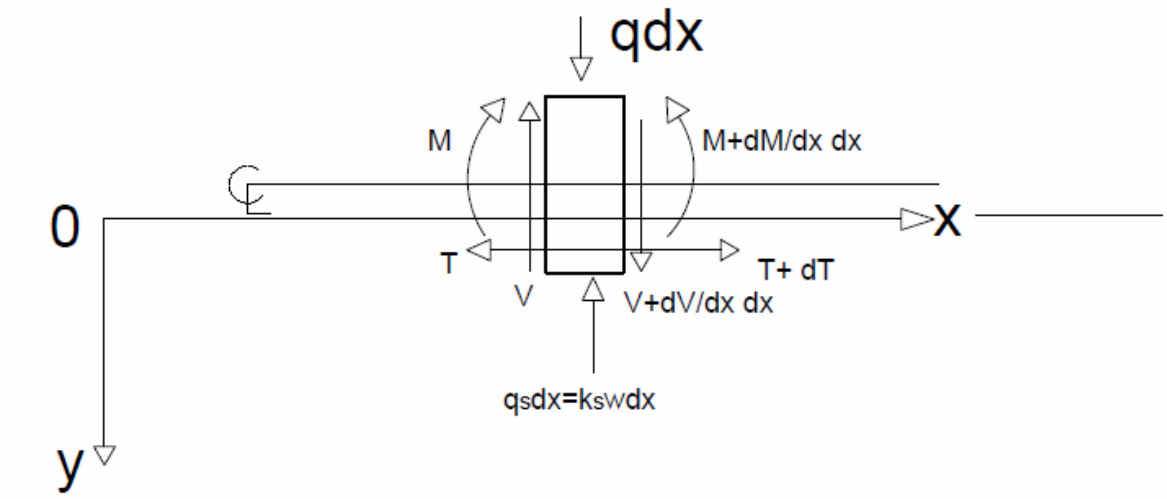

Figure 3. Sign convention for Deflection, Shear Force, Bending Moment, and Tension (Positive as shown).

The vertical fore equilibrium of the beam element in Figure 3 leads to

$$\frac{dQ}{dx} = k_s w - q \tag{3}$$

Where k_s = spring constant in KN/m^3; and q = arbitrary pressure on the beam and may be a function of x. From the moment equilibrium of the beam element

$$\frac{dM}{dx} = Q \tag{4}$$

Using (1) and (2), (3) and (4) can be written as (Yin 2000b)

$$D\frac{d^4w}{dx^4} - \frac{k_s D}{C}\frac{d^2w}{dx^2} + k_s w = q - \frac{D}{C}\frac{d^2q}{dx^2} \tag{5}$$

The bending stiffness D is expressed as

$$D = EI + E_g\left(y_g - y_c\right)^2 \tag{6}$$

Where location of the neutral line y_c, as shown in **Error! Reference source not found.**, can be calculated as

$$y_c = \frac{E_g}{Eh+E_g} y_g \tag{7}$$

Where y_g indicates the location of reinforcement, h is the thickness of the beam as shown in **Error! Reference source not found.**, E is Young's modulus of the beam (kN/m^2) E_g is the tension stiffness of the reinforcement applied in the beam (kN/m), and I is the moment of inertia, which can be calculated as

$$I = \frac{h^3}{12} + hy_c^2 \tag{8}$$

The shear stiffness C can be expressed as (Cowper 1966)

$$C = kG_eA \tag{9}$$

Where G_e is the equivalent shear modulus of the beam with reinforcement. Here, k is a reduction factor which depends on Poisson's ratio υ. Coefficient A is the cross-sectional area, for a unit width, $A = 1 \times h$.

The reinforcement sheet such as geogrid or geotextile in pavement is not considered for shear force but normally considered to take tension only. We can consider shear modulus $G_e = G = 0.5E/(1+\upsilon)$, if the geosynthetic sheets do not take any shear force, G would be the shear modulus of the beam. When reinforcement is considered taking shear force, the shear modulus G_e for shear stiffness shall be calculated as

$$G_e = G + \frac{0.5E_g}{(1+\upsilon_g)A} = G + G_g \quad (10)$$

Where E_g, G_g and υ_g are Young's modulus, shear modulus and Poisson's ratio of the reinforcement, respectively. Yin (2000a) shows that reinforcement tensile force *T* can be expressed as

$$T = -E_g(y_g - y_c)\frac{d\Phi}{dx} \quad (11)$$

1.3 Virtual Load Method (VLM) to Find a Closed-Form Solution of Pavement on Expansive Soils

When the pavement represented as a beam is resting on a regular (unexpansive) soil, it will only deflect by the initiation of an external load. Figure 4 (a) and (b) show the deflection of the beam on the regular soil. Beam deflection on a regular soil can be measured using the Pasternak foundation model. Figure 4 (c) shows beam deflection due to volume change of the subgrade expansive soil. This expansive soil-induced beam deflection can be represented by the introduction of a virtual load on the beam with the subgrade considered as a regular soil. Figure 4 (d) shows the virtual load on a beam with a regular soil as a subgrade. The virtual load makes the beam deflected, which is equivalent to the real deflection induced by the volume change of the expansive soil subgrade. The advantage of this transformation is that this virtual load imposed beam-regular subgrade soil system can be analyzed using the Pastarnak foundation model.

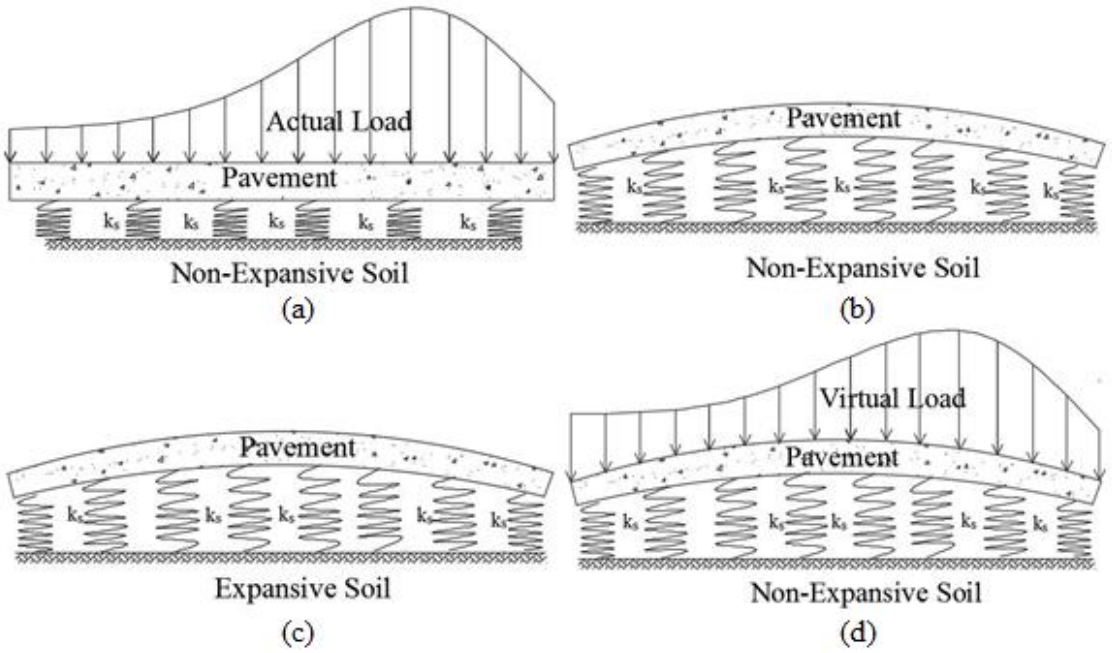

Figure 4. (a) Pavement on a Regular Soil, (b) Pavement Deflection Due to External Load, (c) Pavement Deflection Due to Expansive Soil's Volume Change, and (d) Proposed Virtual Load Soil Model (Adapted from Khan 2017).

1.3.1 The forward analysis of geosynthetic-reinforced pavement on elastic foundation

Let us consider a finite beam (beam length of *L*, bending stiffness D and shear stiffness C) subjected to any form of loading. Then solutions are discovered for the deflection, shear force, and bending moment, etc., at any location along the beam. The process is called a forward analysis. We take pressure *q* as shown in **Error! Reference source not found.**, as the self-weight, any type of external load, or the virtual load that produces equivalent deflection as the heave/shrinkage-induced vertical deformation on pavement, acting over the length of the beam. Load *q* can be expressed as a function of *x*, that is

$$q = f(x) \text{ for } 0 < x < L \tag{12}$$

Where, $f(x)$ can be expressed in a Fourier cosine series.

$$q = \sum_{n=0}^{\infty} A_n \cos\left(\frac{n\pi x}{L}\right) \tag{13}$$

Then Eq. 5 becomes

$$D\frac{d^4w}{dx^4} - \frac{k_s D}{C}\frac{d^2w}{dx^2} + k_s w = \sum_{n=0}^{\infty} A_n \left[1 + \frac{n\pi}{L}\frac{D}{C}\right] cos\frac{n\pi}{L}x \tag{14}$$

By solving this fourth-order nonhomogeneous liner differential equation we can get the beam deflection *w* in terms of Fourier constant A_n. Solution of Eq. 14 is the summation of a homogeneous solution of the beam for any type of load (e.g. a distributed load, or a point load, etc.) and a particular solution which is the function of load type.
Let's assume the particular integral is

$$\mathrm{w_P} = \mathrm{a_n cos}\left(\frac{\mathrm{n}\,\pi\,\mathrm{x}}{\mathrm{L}}\right) \tag{15}$$

From Eq. 14

$$D\left(\frac{\mathrm{n}\,\pi}{\mathrm{L}}\right)^4 \mathrm{a_n cos}\left(\frac{\mathrm{n}\,\pi\,\mathrm{x}}{\mathrm{L}}\right) + \mathrm{k_s}\frac{D}{\mathrm{C}}\left(\frac{\mathrm{n}\,\pi}{\mathrm{L}}\right)^2 \mathrm{a_n cos}\left(\frac{\mathrm{n}\,\pi\,\mathrm{x}}{\mathrm{L}}\right) + \mathrm{k_s a_n cos}\left(\frac{\mathrm{n}\,\pi\,\mathrm{x}}{\mathrm{L}}\right)$$
$$= \mathrm{A_n}\left[1 + \frac{n\pi}{L}\frac{D}{C}\right] \cos\left(\frac{\mathrm{n}\,\pi\,\mathrm{x}}{\mathrm{L}}\right)$$

$$\mathrm{a_n} = \frac{\mathrm{A_n}\left[1+\frac{n\pi D}{L\,C}\right]}{\mathrm{k_s}+\mathrm{k_s}\frac{D}{C}\left(\frac{\mathrm{n}\,\pi}{\mathrm{L}}\right)^2+\mathrm{D}\left(\frac{\mathrm{n}\,\pi}{\mathrm{L}}\right)^4} \tag{16}$$

1.3.2 Beam deflection $W_B(x)$ due to load *q*

A Homogeneous solution of beam for any type of load types (e.g., virtual load, uniformly distributed load (UDL), point load, concentrated moment) is given in Eq. 17 and particular solution which is the function of load type is given in Eq. 65.

$$\mathrm{w_H(x)} = \mathrm{e}^{\alpha\,\mathrm{x}}\{\mathrm{C_1}\cos(\beta\,\mathrm{x}) + \mathrm{C_2}\,\mathrm{sins}(\beta\,\mathrm{x})\} + \mathrm{e}^{-\alpha\,\mathrm{x}}\{\mathrm{C_3}\cos(\beta\,\mathrm{x}) + \mathrm{C_4}\sin(\beta\,\mathrm{x})\} \tag{17}$$

$$\mathrm{w_{PA}(x)} = \mathrm{A_0} + \sum_{\mathrm{n}=1}^{\infty} \mathrm{A_n cos}\left(\frac{\mathrm{n}\,\pi\,\mathrm{x}}{\mathrm{L}}\right) \tag{18}$$

Here, C_1, C_2, C_3, and C_4 are four constants to be determined by the four given boundary conditions.

Solution of Eq. 14 is the summation of the homogeneous solution and the particular solution. Eqs. 19 to 23 show the steps for the beam deflection equation.

$$w_B(x) = w_H(x) + w_{PA}(x) \tag{19}$$

$$w_B(x) = e^{\alpha x}\{C_1 \cos(\beta x) + C_2 \sin(\beta x)\} + e^{-\alpha x}\{C_3 \cos(\beta x) + C_4 \sin(\beta x)\} + \frac{A_0}{k_s} + \sum_{n=1}^{\infty} a_n \cos\left(\frac{n\pi x}{L}\right) \tag{20}$$

Where α and β are the characteristics of the system,

$$\alpha = \sqrt{\sqrt{\frac{k_s}{4D}} + \frac{k_s}{4C}} \tag{21}$$

$$\beta = \sqrt{\sqrt{\frac{k_s}{4D}} - \frac{k_s}{4C}} \tag{22}$$

After rearranging Eq. 20 as a matrix form

$$[w_B(x)] = [e^{\alpha x}\cos(\beta x) \quad e^{\alpha x}\sin(\beta x) \quad e^{-\alpha x}\cos(\beta x) \quad e^{-\alpha x}\sin(\beta x)] * \begin{bmatrix} C_1 \\ C_2 \\ C_3 \\ C_4 \end{bmatrix} + \frac{A_0}{k_s} + \left[\cos\left(\frac{\pi x}{L}\right) \quad \cos\left(\frac{2\pi x}{L}\right) \quad \dots \quad \cos\left(\frac{n\pi x}{L}\right)\right] * \begin{bmatrix} a_1 \\ a_2 \\ \vdots \\ a_n \end{bmatrix} \tag{23}$$

1.3.3 Pavement rotation *Φ(x)* due to *q* load

Eqs. 24 to 27 show the steps for the beam rotation derivations.

$$\phi\,(x) = \frac{dw(x)}{dx} \tag{24}$$

$$\phi\,(x) = e^{\alpha x}\{C_5 \cos(\beta x) + C_6 \sin(\beta x)\} + e^{-\alpha x}\{C_7 \cos(\beta x) + C_8 \sin(\beta x)\} - \sum_{n=1}^{\infty}\left\{\left[\frac{D}{C}\left(\frac{n\pi}{L}\right)^3 - \left(1 - \frac{Dk_s}{C^2}\right)\left(\frac{n\pi}{L}\right)\right] a_n - \frac{n\pi D}{LC^2}A_n\right\}\sin\left(\frac{n\pi x}{L}\right) \tag{25}$$

Where,

$$C_5 = C_1\left[\alpha\left(1 - \frac{Dk_s}{C^2}\right) + \frac{D}{C}(\alpha^3 - 3\alpha\beta^2)\right] + C_2\left[\beta\left(1 - \frac{Dk_s}{C^2}\right) + \frac{D}{C}(3\alpha^2\beta - \beta^3)\right]$$

$$C_6 = C_1\left[-\beta\left(1 - \frac{Dk_s}{C^2}\right) + \frac{D}{C}(-3\alpha^2\beta + \beta^3)\right] + C_2\left[\alpha\left(1 - \frac{Dk_s}{C^2}\right) + \frac{D}{C}(\alpha^3 - 3\alpha\beta^2)\right]$$

$$C_7 = C_3\left[-\alpha\left(1 - \frac{Dk_s}{C^2}\right) + \frac{D}{C}(-\alpha^3 + 3\alpha\beta^2)\right] + C_4\left[\beta\left(1 - \frac{Dk_s}{C^2}\right) + \frac{D}{C}(3\alpha^2\beta - \beta^3)\right]$$

$$C_8 = C_3\left[-\beta\left(1 - \frac{Dk_s}{C^2}\right) + \frac{D}{C}(-3\alpha^2\beta + \beta^3)\right] + C_4\left[-\alpha\left(1 - \frac{Dk_s}{C^2}\right) + \frac{D}{C}(-\alpha^3 + 3\alpha\beta^2)\right]$$

$$\begin{bmatrix} C_5 \\ C_6 \\ C_7 \\ C_8 \end{bmatrix} = \begin{bmatrix} \alpha\left(1-\frac{Dk_s}{c^2}\right)+\frac{D}{c}(\alpha^3-3\alpha\beta^2) & \beta\left(1-\frac{Dk_s}{c^2}\right)+\frac{D}{c}(3\alpha^2\beta-\beta^3) & 0 & 0 \\ -\beta\left(1-\frac{Dk_s}{c^2}\right)+\frac{D}{c}(-3\alpha^2\beta+\beta^3) & \alpha\left(1-\frac{Dk_s}{c^2}\right)+\frac{D}{c}(\alpha^3-3\alpha\beta^2) & 0 & 0 \\ 0 & 0 & -\alpha\left(1-\frac{Dk_s}{c^2}\right)+\frac{D}{c}(-\alpha^3+3\alpha\beta^2) & \beta\left(1-\frac{Dk_s}{c^2}\right)+\frac{D}{c}(3\alpha^2\beta-\beta^3) \\ 0 & 0 & -\beta\left(1-\frac{Dk_s}{c^2}\right)+\frac{D}{c}(-3\alpha^2\beta+\beta^3) & -\alpha\left(1-\frac{Dk_s}{c^2}\right)+\frac{D}{c}(-\alpha^3+3\alpha\beta^2) \end{bmatrix} * \begin{bmatrix} C_1 \\ C_2 \\ C_3 \\ C_4 \end{bmatrix} \quad (26)$$

$$\phi(x) = [e^{\beta x}\cos(\beta x) \quad e^{\beta x}\sin(\beta x) \quad e^{-\beta x}\cos(\beta x) \quad e^{-\beta x}\sin(\beta x)] *$$

$$\begin{bmatrix} \alpha\left(1-\frac{Dk_s}{c^2}\right)+\frac{D}{c}(\alpha^3-3\alpha\beta^2) & \beta\left(1-\frac{Dk_s}{c^2}\right)+\frac{D}{c}(3\alpha^2\beta-\beta^3) & 0 & 0 \\ -\beta\left(1-\frac{Dk_s}{c^2}\right)+\frac{D}{c}(-3\alpha^2\beta+\beta^3) & \alpha\left(1-\frac{Dk_s}{c^2}\right)+\frac{D}{c}(\alpha^3-3\alpha\beta^2) & 0 & 0 \\ 0 & 0 & -\alpha\left(1-\frac{Dk_s}{c^2}\right)+\frac{D}{c}(-\alpha^3+3\alpha\beta^2) & \beta\left(1-\frac{Dk_s}{c^2}\right)+\frac{D}{c}(3\alpha^2\beta-\beta^3) \\ 0 & 0 & -\beta\left(1-\frac{Dk_s}{c^2}\right)+\frac{D}{c}(-3\alpha^2\beta+\beta^3) & -\alpha\left(1-\frac{Dk_s}{c^2}\right)+\frac{D}{c}(-\alpha^3+3\alpha\beta^2) \end{bmatrix} * \begin{bmatrix} C_1 \\ C_2 \\ C_3 \\ C_4 \end{bmatrix} -$$

$$\sum_{n=1}^{\infty}\left\{\left[\frac{D}{c}\left(\frac{n\pi}{L}\right)^3-\left(1-\frac{Dk_s}{c^2}\right)\left(\frac{n\pi}{L}\right)\right]a_n-\frac{n\pi D}{Lc^2}A_n\right\}\sin\left(\frac{n\pi x}{L}\right) \quad (27)$$

1.3.4 Pavement moment *M(x)* due to *q* load

Equations 28 to 31 present the steps of the beam moment equation derivation.

$$\mathrm{M}\,(\mathrm{x}) = -\mathrm{D}\frac{\mathrm{d}\phi(\mathrm{x})}{\mathrm{dx}} \tag{28}$$

$$\frac{\mathrm{d}\phi(\mathrm{x})}{\mathrm{dx}} = \mathrm{e}^{\alpha\,\mathrm{x}}\{\mathrm{C}_9\cos(\beta\,\mathrm{x}) + \mathrm{C}_{10}\sin(\beta\,\mathrm{x})\} + \mathrm{e}^{-\alpha\,\mathrm{x}}\{\mathrm{C}_{11}\cos(\beta\,\mathrm{x}) + \mathrm{C}_{12}\sin(\beta\,\mathrm{x})\} - \sum_{\mathrm{n}=1}^{\infty}\left[-a_n\left(\frac{\mathrm{n}\,\pi}{\mathrm{L}}\right)^2 - a_n\frac{k_s}{c} + \frac{1}{c}A_n\right]\cos\left(\frac{\mathrm{n}\,\pi\,\mathrm{x}}{\mathrm{L}}\right) \tag{29}$$

Where,

$$\mathrm{C}_9 = C_1\left(\alpha^2 - \beta^2 - \frac{k_s}{c}\right) + 2\mathrm{C}_2\alpha\,\beta$$

$$\mathrm{C}_{10} = -2\mathrm{C}_1\alpha\,\beta\; + C_2\left(\alpha^2 - \beta^2 - \frac{k_s}{c}\right)$$

$$\mathrm{C}_{11} = C_3\left(\alpha^2 - \beta^2 - \frac{k_s}{c}\right) - 2\mathrm{C}_4\alpha\,\beta$$

$$\mathrm{C}_{12} = 2\mathrm{C}_3\alpha\,\beta\; + C_4\left(\alpha^2 - \beta^2 - \frac{k_s}{c}\right)$$

They are combined in a matrix format

$$\begin{bmatrix}\mathrm{C}_9\\ \mathrm{C}_{10}\\ \mathrm{C}_{11}\\ \mathrm{C}_{12}\end{bmatrix} = \begin{bmatrix}\left(\alpha^2 - \beta^2 - \frac{k_s}{c}\right) & 2\alpha\,\beta & 0 & 0\\ -2\alpha\,\beta & \left(\alpha^2 - \beta^2 - \frac{k_s}{c}\right) & 0 & 0\\ 0 & 0 & \left(\alpha^2 - \beta^2 - \frac{k_s}{c}\right) & -2\alpha\,\beta\\ 0 & 0 & 2\alpha\,\beta & \left(\alpha^2 - \beta^2 - \frac{k_s}{c}\right)\end{bmatrix} * \begin{bmatrix}\mathrm{C}_1\\ \mathrm{C}_2\\ \mathrm{C}_3\\ \mathrm{C}_4\end{bmatrix} \tag{30}$$

Then the bending moment M(x) could be expressed as

$$M(x) = -D * \Bigg\{ [e^{\alpha x}\cos(\beta x) \quad e^{\alpha x}\sin(\beta x) \quad e^{-\alpha x}\cos(\beta x) \quad e^{-\alpha x}\sin(\beta x)] * \begin{bmatrix} \left(\alpha^2 - \beta^2 - \frac{k_s}{C}\right) & 2\alpha\beta & 0 & 0 \\ -2\alpha\beta & \left(\alpha^2 - \beta^2 - \frac{k_s}{C}\right) & 0 & 0 \\ 0 & 0 & \left(\alpha^2 - \beta^2 - \frac{k_s}{C}\right) & -2\alpha\beta \\ 0 & 0 & 2\alpha\beta & \left(\alpha^2 - \beta^2 - \frac{k_s}{C}\right) \end{bmatrix} * \begin{bmatrix} C_1 \\ C_2 \\ C_3 \\ C_4 \end{bmatrix} - \sum_{n=1}^{\infty}\left[-a_n\left(\frac{n\pi}{L}\right)^2 - a_n\frac{k_s}{C} + \frac{1}{C}A_n\right]\cos\left(\frac{n\pi x}{L}\right) \Bigg\} \quad (31)$$

1.3.5 Pavement shear *Q(x)* due to *q* load

Equations 32 to 35 show the steps of beam shear equation derivation.

$$Q(x) = \frac{dM(x)}{dx} \quad (32)$$

$$Q(x) = D\left[e^{\alpha x}\{C_{13}\cos(\beta x) + C_{14}\sin(\beta x)\} + e^{-\alpha x}\{C_{15}\cos(\beta x) + C_{16}\sin(\beta x)\} + \sum_{n=1}^{\infty}\left[-a_n\left(\frac{n\pi}{L}\right)\frac{k_s}{C} - \left(\frac{n\pi}{L}\right)^3 a_n + \frac{n\pi}{CL}A_n\right]\sin\left(\frac{n\pi x}{L}\right)\right] \quad (33)$$

Where,

$$C_{13} = C_1\left(\alpha\frac{k_s}{C} - \alpha^3 + 3\alpha\beta^2\right) + C_2\left(\beta\frac{k_s}{C} - 3\alpha^2\beta + \beta^3\right)$$

$$C_{14} = C_1\left(-\beta\frac{k_s}{C} + 3\alpha^2\beta - \beta^3\right) + C_2\left(\alpha\frac{k_s}{C} - \alpha^3 + 3\alpha\beta^2\right)$$

$$C_{15} = C_3\left(-\alpha\frac{k_s}{c} + \alpha^3 - 3\alpha\beta^2\right) + C_4\left(\beta\frac{k_s}{c} - 3\alpha^2\beta + \beta^3\right)$$

$$C_{16} = C_3\left(-\beta\frac{k_s}{c} + 3\alpha^2\beta - \beta^3\right) + C_4\left(-\alpha\frac{k_s}{c} + \alpha^3 - 3\alpha\beta^2\right)$$

$$\begin{bmatrix} C_{13} \\ C_{14} \\ C_{15} \\ C_{16} \end{bmatrix} =$$

$$\begin{bmatrix} \left(\alpha\frac{k_s}{c} - \alpha^3 + 3\alpha\beta^2\right) & \left(\beta\frac{k_s}{c} - 3\alpha^2\beta + \beta^3\right) & 0 & 0 \\ \left(-\beta\frac{k_s}{c} + 3\alpha^2\beta - \beta^3\right) & \left(\alpha\frac{k_s}{c} - \alpha^3 + 3\alpha\beta^2\right) & 0 & 0 \\ 0 & 0 & \left(-\beta\frac{k_s}{c} + 3\alpha^2\beta - \beta^3\right) & \left(\beta\frac{k_s}{c} - 3\alpha^2\beta + \beta^3\right) \\ 0 & 0 & \left(-\beta\frac{k_s}{c} + 3\alpha^2\beta - \beta^3\right) & \left(-\alpha\frac{k_s}{c} + \alpha^3 - 3\alpha\beta^2\right) \end{bmatrix} *$$

$$\begin{bmatrix} C_1 \\ C_2 \\ C_3 \\ C_4 \end{bmatrix} \qquad (34)$$

$$Q(x) = D * \Bigg[[e^{\alpha x}\cos(\beta x) \quad e^{\alpha x}\sin(\beta x) \quad e^{-\alpha x}\cos(\beta x) \quad e^{-\alpha x}\sin(\beta x)] * \begin{bmatrix} \left(\alpha\frac{k_s}{C} - \alpha^3 + 3\alpha\beta^2\right) & \left(\beta\frac{k_s}{C} - 3\alpha^2\beta + \beta^3\right) & 0 & 0 \\ \left(-\beta\frac{k_s}{C} + 3\alpha^2\beta - \beta^3\right) & \left(\alpha\frac{k_s}{C} - \alpha^3 + 3\alpha\beta^2\right) & 0 & 0 \\ 0 & 0 & \left(-\beta\frac{k_s}{C} + 3\alpha^2\beta - \beta^3\right) & \left(\beta\frac{k_s}{C} - 3\alpha^2\beta + \beta^3\right) \\ 0 & 0 & \left(-\beta\frac{k_s}{C} + 3\alpha^2\beta - \beta^3\right) & \left(-\alpha\frac{k_s}{C} + \alpha^3 - 3\alpha\beta^2\right) \end{bmatrix} * \begin{bmatrix} C_1 \\ C_2 \\ C_3 \\ C_4 \end{bmatrix} + \sum_{n=1}^{\infty}\left[-a_n\left(\frac{n\pi}{L}\right)\frac{k_s}{C} - \left(\frac{n\pi}{L}\right)^3 a_n + \frac{n\pi}{CL}A_n\right]\sin\left(\frac{n\pi x}{L}\right)\Bigg] \tag{35}$$

1.3.6 Boundary conditions

Applying boundary conditions, $M|_{x=0} = 0$, $Q|_{x=0} = 0$, $M|_{x=L} = 0$, $Q|_{x=L} = 0$, to Eqs. 31 and 35, and after mathematical manipulations, they can be written in the matrix template $[M]\{c\} = [R]$. Matrix **M** is a function of basic parameters such as α, β, L, k_s, D, I and C, where **R** is a function of parameters for load **q** (e.g. [a_1 a_2 … a_n]). Using matrix $\{c\} = [M]^{-1}[R]$, constants C_1 through C_4 can be discovered as a function of parameters for load **q** (e.g. [a_1 a_2 … a_n]). Following the similar procedure of matrix manipulations done by Khan and Wang (2017), Eq. 20 can be reduced into a combination of a set of linear equations. Eq. 36 shows the final matrix solution of the beam deflection. Here, matrix element $\boldsymbol{H_n}$ is a function of basic parameters such as α, β, L, k_s, D, I and C. Repeating the same procedure matrix solutions can be developed for rotation, moment and shear force, respectively.

$$[w(x)] = \begin{bmatrix} \frac{1}{k_s} & H_1 & H_2 & \dots & H_n \end{bmatrix} \begin{bmatrix} A_0 \\ a_1 \\ a_2 \\ \vdots \\ a_n \end{bmatrix} \tag{36}$$

$$[\boldsymbol{M}][\boldsymbol{C}] = [\boldsymbol{R}]$$

$$\begin{bmatrix} \left(\alpha^2 - \beta^2 - \frac{k_s}{c}\right) & 2\alpha\,\beta & \left(\alpha^2 - \beta^2 - \frac{k_s}{c}\right) & -2\alpha\,\beta \\ \left(\alpha\frac{k_s}{c} - \alpha^3 + 3\alpha\beta^2\right) & \left(\beta\frac{k_s}{c} - 3\alpha^2\beta + \beta^3\right) & \left(-\alpha\frac{k_s}{c} + \alpha^3 - 3\alpha\beta^2\right) & \left(\beta\frac{k_s}{c} - 3\alpha^2\beta + \beta^3\right) \\ \left(\alpha^2 - \beta^2 - \frac{k_s}{c}\right) e^{\alpha L}\cos(\beta\,\mathrm{L}) - 2\alpha\,\beta\; e^{\alpha L} sin(\beta L) & 2\alpha\,\beta\; e^{\alpha L} cos(\beta L) + \left(\alpha^2 - \beta^2 - \frac{k_s}{c}\right) e^{\alpha L}\sin(\beta\,\mathrm{L}) & \left(\alpha^2 - \beta^2 - \frac{k_s}{c}\right) e^{-\alpha L}\cos(\beta\,\mathrm{L}) + 2\alpha\,\beta\; e^{-\alpha L} sin(\beta L) & -2\alpha\,\beta\; e^{-\alpha L} cos(\beta L) + \left(\alpha^2 - \beta^2 - \frac{k_s}{c}\right) e^{-\alpha L}\sin(\beta\,\mathrm{L}) \\ e^{\alpha L}\left\{\left(\alpha\frac{k_s}{c} - \alpha^3 + 3\alpha\beta^2\right)cos(\beta L) + \left(-\beta\frac{k_s}{c} + 3\alpha^2\beta - \beta^3\right)sin(\beta L)\right\} & e^{\alpha L}\left\{\left(\alpha\frac{k_s}{c} - \alpha^3 + 3\alpha\beta^2\right)sin(\beta L) + \left(\beta\frac{k_s}{c} - 3\alpha^2\beta + \beta^3\right)cos(\beta L)\right\} & e^{-\alpha L}\left\{\left(-\alpha\frac{k_s}{c} + \alpha^3 - 3\alpha\beta^2\right)cos(\beta L) + \left(-\beta\frac{k_s}{c} + 3\alpha^2\beta - \beta^3\right)sin(\beta L)\right\} & e^{-\alpha L}\left\{\left(-\alpha\frac{k_s}{c} + \alpha^3 - 3\alpha\beta^2\right)sin(\beta L) + \left(\beta\frac{k_s}{c} - 3\alpha^2\beta + \beta^3\right)cos(\beta L)\right\} \end{bmatrix} \begin{bmatrix} C_1 \\ C_2 \\ C_3 \\ C_4 \end{bmatrix} =$$

$$\begin{bmatrix} \sum_{n=1}^{4}\left[a_n\left(\frac{n\pi}{L}\right)^2 + a_n\frac{k_s}{c} - \frac{1}{c}A_n\right] \\ 0 \\ \sum_{n=1}^{4}\left[a_n\left(\frac{n\pi}{L}\right)^2 + a_n\frac{k_s}{c} - \frac{1}{c}A_n\right](-1)^n \\ 0 \end{bmatrix} \tag{37}$$

$$[\boldsymbol{C}] = [\boldsymbol{M}]^{-\mathbf{1}}[\boldsymbol{R}] = [\boldsymbol{D}][\boldsymbol{R}]$$

1.3.7 The inverse analysis of geo-synthetic reinforced pavement on expansive soils

The research that has been conducted is to find shear stress and bending moment, etc., across the geosynthetic-reinforced pavement, which is placed on expansive subgrade soils. Heave or shrinkage produces the pavement deflections, and then results in shear force and bending moment in the pavement. As described in Khan and Wang (2017), the VLM is performed by finding a virtual distributed load that is applied on the pavement. The virtual load generates pavement (beam) deflections. To find the unknown virtual load, as described before, the load is expressed as the summation of a Fourier series, with a group of unknown load parameters to be identified. To do so, the inverse theory is applied.

In the inverse analysis, the model parameters are estimated by minimizing a 'norm' of the difference between observed and model-estimated values at predetermined observation points. In this research, as it was done in Khan (2017), a set of heave/shrinkage-induced vertical displacements in the underlain expansive subgrade soils, which are indicated by $\boldsymbol{W_P}$, are predicted based on the unsaturated mechanics. It is regarded as the observed output. The estimated pavement/beam deflections are taken as $\boldsymbol{W_B}$. The observation data can be related to the model estimated values at the predetermined points by the following relationship

$$W_P = W_B(\ \chi \mid \zeta\ ) + \boldsymbol{\varepsilon} \tag{38}$$

Where, $\boldsymbol{\chi}$ represents the known input data matrix, which is a function of basic parameters such as α, β, L, k_s, D, I and C.

Model parameter vector, $\zeta = \begin{bmatrix} A_0 \\ a_1 \\ a_2 \\ \vdots \\ a_n \end{bmatrix}$

And, $\boldsymbol{\varepsilon}$ is the error vector.

Here, the linear least square method is used and a general approach to the least square problem is to make $\left|\left|\varepsilon\right|\right|^2$ minimal. The sum of the squared differences (SSE) can be obtained by

$$SSE = \left|\left|\varepsilon\right|\right|^2 = \left|\left|W_p - W_B(\chi \mid \zeta)\right|\right|^2 \quad (39)$$

The algebraic solution of the normal equation can be written as

$$\zeta = (\chi^T \chi)^{-1} \chi^T W_P \quad (40)$$

Once $\boldsymbol{\zeta}$ is found, using Eq. 36 we can calculate the beam deflection produced by the virtual load along the pavement cross-section. Then, values of $\boldsymbol{\zeta}$ can be used to determine all the Fourier constants by using Eq. 16 and by employing Fourier constants into Eq. 13 we will find the virtual load imposed along the pavement cross-section. After that, using matrix $\{c\} = [M]^{-1}[R]$ (Eq. 37) constants C_1 through C_4 can be found. As soon as C_1 through C_4 becomes available constant C_5 through C_{16} can be obtained using Eqs. 26, 30, and 34. Finally, all the parameters stated above will be identified thus rotation, moment, shear force at any cross section of the beam/pavement, and tensile force acting upon geosynthetic can be acquired using Eqs. 27, 31, 35 and 11, respectively.

2. The Reinforcement Effect of Geosynthetics on the Pavement of Research Road FM 2, TX, USA

The pavement of a country road called FM 2 (farm to market road No. 2), on which a one-year long field research was conducted by TxDOT, was selected to analyze the damage caused by the expansive subgrade soil by applying the Virtual Load Method. Texas FM 2 is situated in Grimes County, which is southeast side of Texas. **Error! Reference source not found.** shows the location of FM 2, relative to other major cities in Texas. The entire pavement was divided into 32 test sections, and moisture content sensors were installed at different stations (Zornberg et al. 2008). According to 'web soil survey' by Natural Resources Conservation Service (NRCS) of United States Department of Agriculture, the Frelsburg clay is located at the FM 2 site. With its liquid limit (90) and plasticity index (65), the Frelsburg clay was clearly classified as a highly expansive clay.

Figure 5. Location and layout of FM 2 relative to major metropolitan areas in Texas.

Geogrids were used as reinforcement materials for the pavements of FM 2. Based on the preliminary investigation and the TxDOT requirements, test sections were reconstructed at FM 2 site. To prevent longitudinal cracking, TxDOT used lime stabilization in the subgrade and geogrid reinforcement at the interface between the subgrade and base course. Part of this study was to compare the effectiveness of geogrid and geotextile to prevent translation of the expansive displacements in the subgrade into the base course.

2.1 Vertical deformation of the subgrade expansive soil

Deformation of the subgrade expansive soil is a function of moisture content fluctuation in the soil due to climate changes, and it affects the pavement resting on expansive soil. Time dependent moisture content profiles from below the pavement center to the ditch center were extracted through multiple moisture sensors installed at the FM 2 project site near College Station, TX, which was investigated by TxDOT, and documented in Zornberg et al. (2008). Field measurements showed an increasing trend of moisture fluctuations from the pavement center to the ditch. From the thirty-year climate data of the pavement location, the driest and wettest months were found in July and September, respectively. In this study, the theoretical moisture distributions of July and September were taken to replicate extreme shrinkage and extreme heave condition, respectively. Ikra (2017) simulated the moisture distribution and calculated the heave and shrinkage-induced vertical deformation of the subgrade expansive soils subjected to the extreme shrinkage or heave conditions, respectively. They were plotted on the top left parts of Figure 7 andFigure 8, as “measured heave” and “measured shrinkage”, respectively. Khan (2017) adopted the distribution of moisture content and the subsequent subgrade deformations across the cross-section of the pavement for the analysis of the reinforcement-free pavement using the developed virtual load method. It is worthwhile to note that the “measured heave/shrinkage” was a conservative estimate of “free heave/shrinkage”, which implies that the expansive subgrade soils expands or shrinks underneath the pavement subjected to a zero vertical pressure condition. Stiffness of the reinforced pavement will apply certain amount of restriction to the deformation of the subgrade soils, which will definitely reduce the heave/shrinkage-induced pavement deflections. In this research, the virtual load method is still performed based on the free heave/shrinkage deformation. Research is in progress on the virtual load method for the reinforced pavement considering the pavement restriction on the deformation of the expansive subgrade soils.

2.2 Material properties of the pavement-foundation system

In this case study, the geosynthetic-reinforced pavement is investigated. It is simplified as a reinforced Timoshenko beam resting on expansive soil, as shown in

Figure 6. The structural properties of the beam are defined in Table 1. A typical value of the Young's modulus *E* for a pavement is in the range of 10,000 kPa to 200,000 kPa. Since the pavement is placed on the expansive soil, it is hard to compact the granular soil of the pavement to a high density to attain a high stiffness. For this case study, the young's modulus *E* is taken to be 50 MPa. Young's modulus E_{clay} for the expansive subgrade clay can be defined from its undrained shear strength C_u (Yin 2000b). Researchers have discussed the validation and estimation of spring constant k_s, which is known as Modulus of subgrade reaction, and it can be determined by using Eq. 41 (Selvadurai 1979; Terzaghi 1955; Vesic 1961). From Table 1, the k_s value for analyzing soil heave/shrinkage (B=L) is found to be 2.67×10^2 kN/m^3. Here, *L* is the width of the FM 2 road, and v_s is the Poisson's ratio of expansive soil.

Table 1 Material properties of the pavement-foundation framework

Length of the Pavement, L (m)	10	Location of the geosynthetic, y_g (m)	0.24
Height of the pavement, h (m)	0.64	Location of neutral line, y_c (m)	0.146
Modulus of Elasticity of Pavement, E (kN/m^2)	50,000	Tension Modulus of Geosynthetics, E_g (kN/m)	50,000
Poisson's ratio, υ	0.3	Modulus of Elasticity of Expansive clay, E_{clay} (kN/m^2)	2,000

$$k_s = \frac{E_{clay}}{B(1-v_s^2)} \tag{41}$$

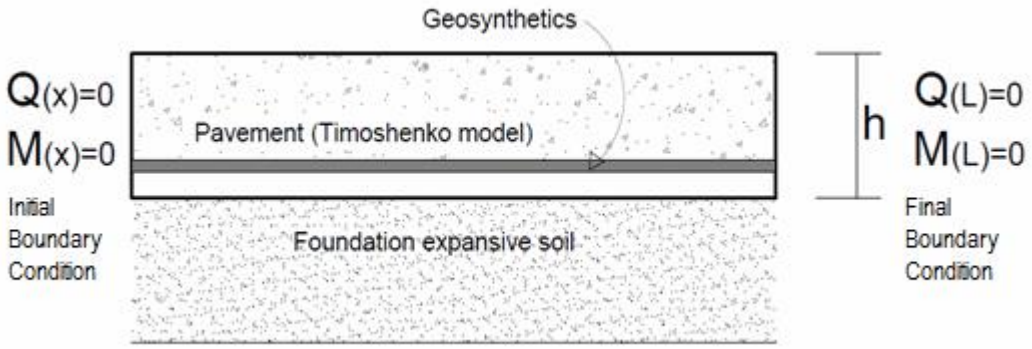

Figure 6 A schematic diagram of a typical geosynthetic-reinforced pavement on expansive soil.

2.3 Analysis of geosynthetic-reinforced pavement due to extreme soil heave/shrinkage condition

Numerical studies were performed by carefully selecting a group of material parameters. Solutions of bending moments, shear forces and tensile forces through the geosynthetics are presented in this section for extreme shrinkage and heave conditions, respectively in this report. Geotextiles and geogrids with a high modulus of elasticity are used in this study as the soil reinforcing elements in the geosynthetic-reinforced pavement. The tension modulus E_g of geosynthetics in reinforcement application is in the range of 20 to 7000 kN/m. For this case study, E_g was taken as 50 MN/m to analyze the pavement on expansive soils. Geosynthetic reinforcement in the pavement layers improves the performance of the transport support. However, it is necessary to evaluate the optimum location of the geosynthetics based upon the tensile force. To make this study simpler, location of the geosynthetics, y_g was selected 0.24 m below the center line of the pavement as depicted in **Error! Reference source not found.**.

The effects of the geosynthetic shear stiffness G_g were investigated in this study. For geogrid sheets, their shear stiffness was taken into account. A full scale of G_g was employed for all the analyses. On the other hand, for geotextile sheets, they do not take any shear force, so G_g is assumed to be zero. To evaluate the effect of the shear stiffness of the pavement, shear coefficient k is needed. In this study, a rectangular cross-section is assumed for the pavement. k is independent of the aspect ratio (ratio of the pavement thickness to its width). When Poisson's ratio u varies between 0 and 0.5, k fluctuates in the range between 0.833 and 0.857 (Cowper 1966), and in case of a thin beam between 0.833 and 0.882 (Stephen 1980).

Maximum and minimum values of shear force and bending moment on pavement and tension force through the geosynthetics are presented in Table 2 for the extreme shrinkage or heave condition. Virtual loads, rotations, shear forces and bending moments on the cross sections, and tensile forces through the geosynthetics reinforcement along the beam/pavement width direction are plotted in Figure 7 and Figure 8. Results with the condition of $G_g = 0$ are for the geotextile

condition, and those with a full scale of G_g for the geogrid condition. From top-left pars of Figure 7Figure 8, it can be observed that the calculated Timoshenko beam deflections from the virtual loads for the shrinkage or heave conditions agreed well with the “measured” shrinkage or heave-induced vertical deformations. It is found that, under the extreme shrinkage condition, for the geogrid-reinforced pavement, the maximum shear force was 53% higher than that for the geosynthetic-reinforced pavement, the maximum bending moment 26% higher, and the maximum tension force 26% higher. Under the extreme heave condition, for the geogrid-reinforced pavement, the maximum shear force was 51% higher than that for the geosynthetic-reinforced pavement, the maximum bending moment 58% higher, and the maximum tension 54% higher. It is concluded that the geosynthetic-reinforced pavement resting on the expansive subgrade can resist more shear force or bending moment when the geosynthetic shear stiffness is considered. The tension without considering geosynthetic shear stiffness (e.g. geotextile) is smaller than in the case where geosynthetic shear stiffness (e.g. geogrid) is considered.

Table 2 Maximum and minimum rotation, shear, and moment on pavement and tension in geosynthetics for Texas FM 2 research road by applying the VLM

Different conditions			Shear (kN/m)	Moment (kN-m/m)	Tension (kN/m)
Extreme Shrinkage	Max	Full G_g	1571	518	1099
Extreme Shrinkage	Max	Zero G_g	736	385	816
Extreme Shrinkage	Min	Full G_g	-1571	0	0
Extreme Shrinkage	Min	Zero G_g	-736	0	0
Extreme Heave	Max	Full G_g	165	19	39
Extreme Heave	Max	Zero G_g	81	8	18
Extreme Heave	Min	Full G_g	-165	-78	-166
Extreme Heave	Min	Zero G_g	-81	-57	-121

Table 3 presents the variations of the tension forces due to the effect of geosynthetic tension modulus E_g , which varied in the research in four stages: 0, 1000, 5000, and 50000 kN/m) with and without shear stiffness for extreme heave and/or shrinkage conditions, respectively. When the tension modulus E_g of the reinforcement is 0, it corresponds to the reinforcement-free case. Figure 8 shows that, for the extreme shrinkage condition, with the increasing value of tension

modulus E_g, an increase in tension force is expected, whereas the peak virtual load intensity decreases, and vice versa. On the other hand, Figure 7 shows that, for the extreme heave condition, with the increasing value of tension modulus E_g, an increase in tension is obtained, whereas the peak virtual load intensity increases, and vice versa. Preliminary analyses ended up with the following explanations. For the reinforcement-free scenario, E_g becomes 0, and the peak virtual load is equal to 5426 kPa for the extreme shrinkage condition, and 1268 kPa for the extreme heave condition. When the pavement is reinforced with geosynthetic, with E_g considered as 50,000 kN/m, the maximum tensile force in the reinforcement is 1099 kN/m if geogrid is used for the extreme shrinkage condition and 39 kN/m for the extreme heave condition. Results for the geogrid and geotextile cases are compared in table 3 where E_g varies four times from zero to 50,000 kN/m. It shows that the peak virtual load intensity with the geogrid case increases by 47% for the extreme shrinkage condition, and 39% for the extreme heave condition if the geosynthetic tensile modulus E_g increases from 0 to 50,000 kN/m. It indicates that the capability of geosynthetics to withstand the induced stresses from the volume changes of the expansive subgrade soils.

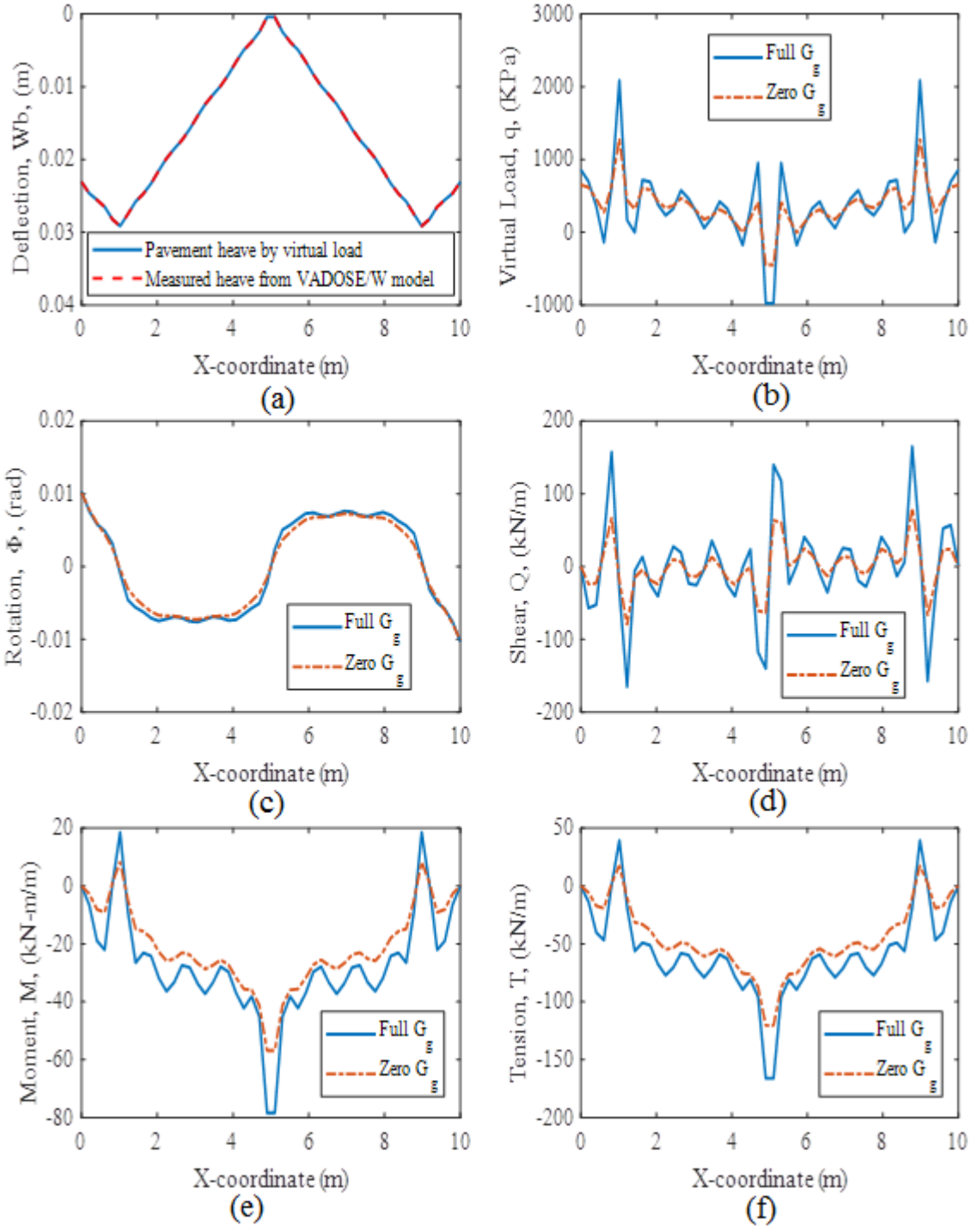

Figure 7. (a) Deflection, (b) virtual load, (c) rotation, (d) shear, (e) bending moment and (f) tension force diagrams for extreme heave condition.

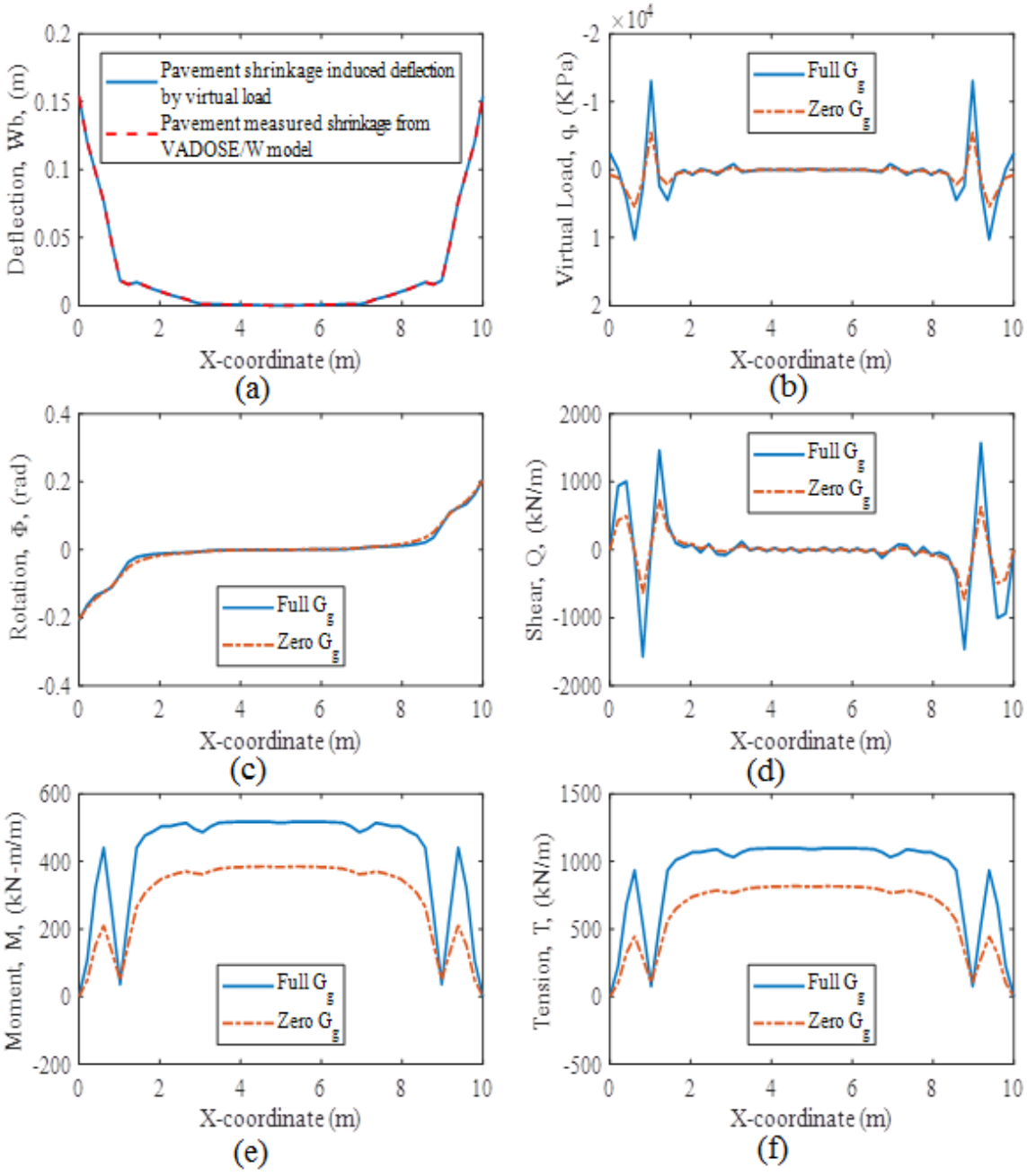

Figure 8. (a) Deflection, (b) virtual load, (c) rotation, (d) shear, (e) bending moment and (f) tension force diagrams for extreme shrinkage condition.

Table 3 Tensile force and virtual load variation of Texas FM 2 road with and without geosynthetics.

Tension Modulus of Geosynthetics, E_g (KN/m)	*	0	0	1000	1000	5000	5000	50000	50000
Tension Modulus of Geosynthetics, E_g (KN/m)	*	Virtual Load (kPa)	Tension (kN/m)	Virtual Load (kPa)	Tension (kN/m)	Virtual Load (kPa)	Tension (kN/m)	Virtual Load (kPa)	Tension (kN/m)
Extreme Shrinkage	Max Full G_g	5426	0	5533	18	5954	91	10298	1099
Extreme Shrinkage	Max Zero G_g	5426	0	5428	17	5435	87	5494	816
Extreme Shrinkage	Min Full G_g	-5405	0	-5570	0	-6223	0	-13046	0
Extreme Shrinkage	Min Zero G_g	-5405	0	-5409	0	-5421	0	-5539	0
Extreme Heave	Max Full G_g	1268	0	1285	0	1355	2	2088	39
Extreme Heave	Max Zero G_g	1268	0	1268	0	1269	2	1283	18
Extreme Heave	Min Full G_g	-432	0	-444	-3	-492	-13	-976	-166
Extreme Heave	Min Zero G_g	-432	0	-433	-3	-434	-13	-448	-121

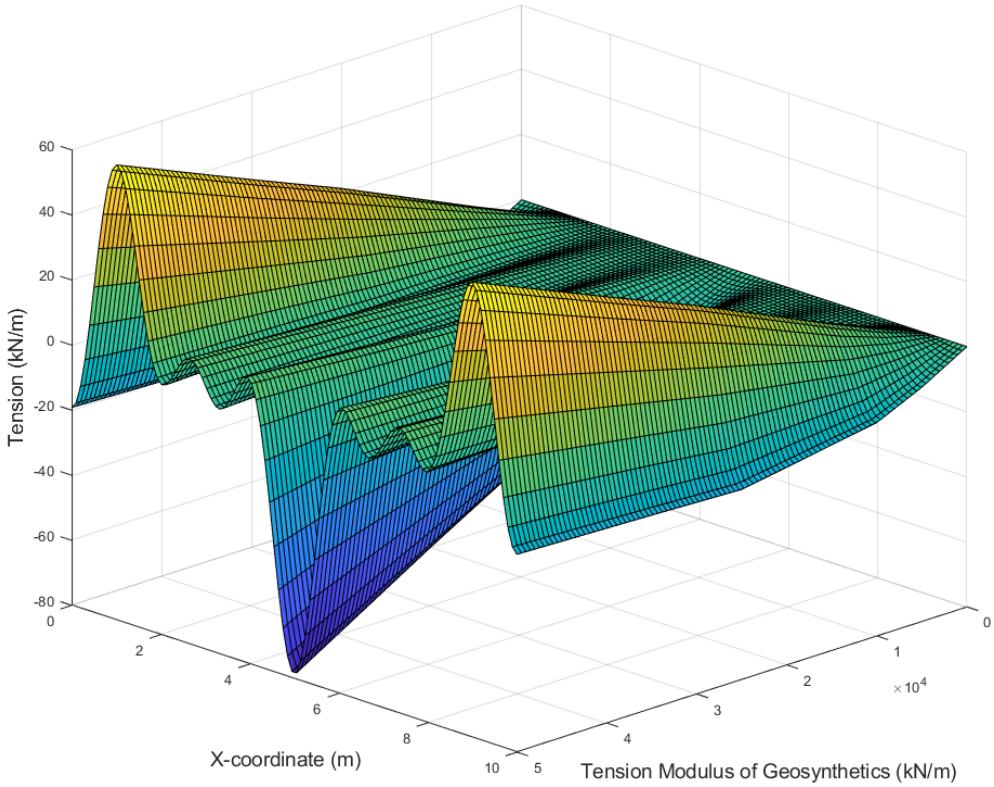

Figure 9. Constitutive tension surface for geosynthetic-reinforcement (Extreme heave).

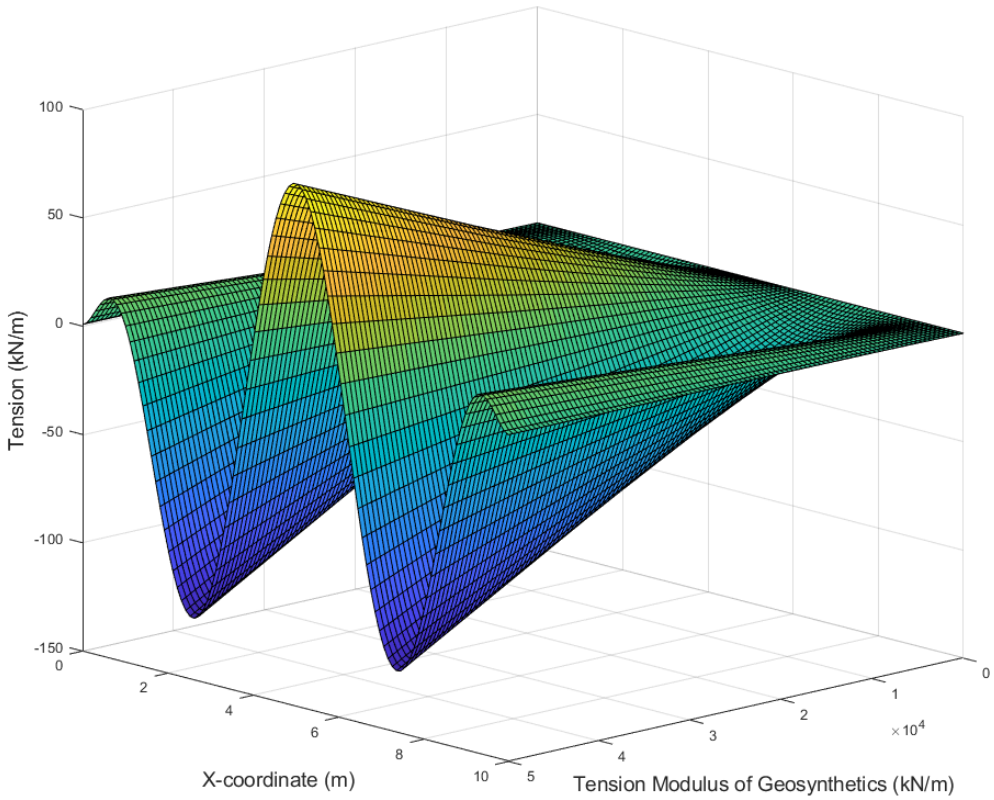

Figure 10. Constitutive tension surface for geosynthetic-reinforcement (Extreme shrinkage).

From Figure 9 and 10, we can establish the variation of Tension force applied on the geosynthetics due to deflection of the beam with the increment of Tension Modulus of Geosynthetics for FM 2 road, TX. From Figure 9, it can be identified that the maximum positive tension force was increasing on “both shoulder” of the pavement for extreme heave condition. On the other hand, from Figure 10, we can see the maximum positive tension was increasing at the “middle” of the pavement with the increase of Tension Modulus of geosynthetic for extreme shrinkage condition. We can state that, geosynthetic can perform a vital role by carrying tension force at the middle of the pavement resting on expansive subgrade during dry season.

3. Numerical Prediction of Moisture Fluctuations in Unsaturated Expansive Clay and Heave Analysis under Extreme Weather Conditions

3.1 INTRODUCTION

The expansive soil problem is very common throughout the world and severe in the United States, Australia, Canada, China, India, and South Africa (Chen 1988), and it can be considered as one of the most common reasons causing pavement/foundation distress. Investigations (Puppala et al. 2009) showed that the damage cost on lightly loaded foundations/pavements caused by expansive soils was as high as $13 billion per year. Due to the presence of highly plastic mineral montmorillonite expansive soils exhibit significant volume changes with the variation in water content (Adem 2015). Over many years, especially in last 15 years many researchers have proposed various methods for predicting soil heave over time (Adem 2015; Adem and Vanapalli, 2013; Alonso et al. 1990; Briaud et al. 2003; Nelson et al. 2007; Overton et al. 2006; Vu and Fredlund 2006; Wray et al. 2005; and Zhang 2004). In any method predicting volume change of expansive soils over time the prediction of water content or soil suction fluctuations is usually made. Although the volume change phenomenon due to climate change over time is more correlated to suction change in the soil, water content prediction is more dependable and easier than matric suction (Marr et al. 2004). In last few decades, significant achievements have been made about numerical modeling of moisture movement in unsaturated soils. Numerical schemes and algorithms have been developed to model the moisture flow, which has made the finite element analyses feasible and implementable in engineering practice. In the finite element analyses, environmental and seasonal changes, such as precipitation, air temperature, and seepage and drainage conditions could be taken into account to a large extent.

Application of VADOSE/W in predicting the moisture content changes in the expansive soils below pavement has provided good approximations as compared with field measured moisture content data (Overton et al. 2006). FlexPDE, PLAXFLOW, and SUCH are some other numerical software programs, which were used for predicting suction/water content fluctuations in soils. FlexPDE could

integrate structural loads in the analyses of moisture fluctuations (Vu and Fredlund 2004). Vu and Fredlund (2004) successfully predicted the time-dependent matric suction change with depth using FlexPDE in the expansive soils below the concrete slab under a building in Saskatchewan, Canada.. The construction of a building took place during August 1961. One year after building in August 1962, the owner of that building observed heave and cracking of the floor slab. The cracking was caused by the volume change of the expansive soils due to the leakage of a hot water line under the floor slab. The numerical analyses and field investigation both confirmed the cause. All the details on testing and monitoring of the site were documented by Yoshida *et al*. (1983). This numerical result was validated through VASOSE/W using the same properties used by Vu and Fredlund, 2004 (Ikra 2017). The research purpose is to analyze the water content change, and to predict the free heave/shrinkage without considering the effect of structural and traffic loads. Soil-water interaction with the changes in environmental conditions was considered in this study. Among the numerical tools VADOSE/W was taken the most reliable for this study because, it can include the climate effect (the maximum and minimum temperature, precipitation, wind speed, evaporation, duration of rainfall, latitude of the area to ensure orientation of sun) in every step of the simulations. VADOSE/W is the only 2-D package that can generate realistic evaporation based on the latitude information. In addition, VADOSE/W is capable of analyzing the vegetation, root transpiration, runoff and ponding (Booth 2014).

Unsaturated soil problems with climatic interactions are often conducted as a 2-D problem. The VADOSE/W analysis requires the following input information: (i) material properties, namely the soil-water characteristic curve (SWCC), and the coefficient of permeability function (k function), (ii) climate data including the daily precipitation, the maximum and minimum daily temperature, the maximum and minimum daily relative humidity, the average daily wind speed, and the net radiation, (iii) vegetation data which involves the leaf area index (LAI), the plant moisture limiting point, the root depth and length in the growing season, and (iv) geometrical boundary conditions including the location of the ground water table (Geo-slope 2007).

For the simulation of unsaturated flow, it is important to define the accurate boundary and initial condition. The boundary conditions which are generally used in VADOSE/W are often applied at the bottom of the soil profile include unit gradient, seepage face (flux), and pressure head. The initial condition is also required for the simulation of the transient water flow through unsaturated soils. VADOSE/W permits to specify the initial hydraulic conditions by either creating an initial condition file in a separate analysis, or by drawing the initial water table position or by specifying the value as a material property. The output of VADOSE/W includes the soil temperature, degree of saturation, water content, and, most importantly, matric suction fluctuations over time.

After the water content change was analyzed through the numerical model, the heave/shrinkage can be predicted. In this research, the extensively accepted equations Richards (1967) and Dhowian (1990) were used to predict the volume change because of moisture content fluctuation.

Richards (1967) equation:

$$\Delta H = \sum \frac{H}{3} \frac{(w_f - w_i)G_S}{(100 + w_i G_S)} \quad (42)$$

Dhowian (1990) equation:

$$\Delta H = H \frac{\alpha\, G_S}{1 + e_0} (w_f - w_i) \quad (43)$$

where ΔH= Heave

H= thickness of each layer

e_o= initial void ratio

w_i= initial water content

w_f= final water content

G_s= specific gravity of soil

α= volume compressibility index

These two equations were used for heave/shrinkage prediction of the expansive clays, in which the variable final water content w_f was the outcome of VADOSE/W analysis.

Expansive soils in semi-dry and dry regions are experienced with moisture fluctuation due to seasonal variations resulting in large volumetric changes in the expansive subgrade soils. The volume changes caused the periodic heave/shrinkage of the pavements. Texas Department of Transportation (TXDOT) addressed in the report (Zornberg et al. 2008) that these periodical movements caused remarkable damage in the form of longitudinal cracks on the pavement. TXDOT conducted different surveys on different pavements to understand the possible cause of longitudinal cracking (Zornberg et al. 2008). After gathering the experience from the field monitoring results from different pavements, and in order to formulate the seasonal variations of moisture content in the expansive soils below the pavements, TXDOT conducted a two-year long field research project, in an effort to directly measure the moisture content variations in the expansive soils. The reconstruction of a country road called Farm-to-Market No. 2 (FM 2) in Bryan district of Texas was selected for the field research (Zornberg et al. 2008).

To observe the moisture fluctuations TXDOT installed both horizontal and vertical moisture sensors below the pavement during its construction. In the project, a series of moisture sensors (horizontal and vertical) were installed at different locations of the project area. In this study, moisture sensors data obtained from FM 2 field were used extensively to develop a moisture flow model to analyze long-term moisture fluctuations. The horizontal array of the sensors showed the movements of water below the pavement and vertical arrays were useful to evaluate the moisture fluctuations in the soil profile without the effect of pavement boundary. Vertical sensors were installed at stations 184 and 199, which were located below the ditches at two sides of the pavement. Horizontal sensors were located below the pavement from pavement center to ditch center. The field research ended up with a large amount of field measurements of moisture contents through the expansive subgrade soils, which could be employed for an effective validation of the numerical model.

In this research, a VADOSE/W-based numerical model was established to study the water content change of the expansive soils below the pavements in the FM 2 field research project. The boundary flux conditions were estimated considering the detailed climatic condition collected at a weather station near the test site. Soil properties and initial suction conditions for the modeling were obtained from the TXDOT detailed project evaluation report (Zornberg et al. 2008). After calibrating the model against field data, a validation study of water content fluctuations in the subgrade clay soils was conducted for the climatic conditions over a period of one year from February 2, 2006, to February 1, 2007. Results were also analyzed from paved and unpaved soil profile to understand the impact of the pavement due to moisture fluctuations. Heave/shrinkage prediction was also considered in this study. To analyze the soil ground movement, two extreme weather (driest and wettest times) conditions in the year were considered.

In the SPTC-funded project, this part of research was focused on the numerical prediction of moisture content fluctuation in expansive clay leading to volume change due to climate changes and its effect on the pavement sitting on expansive soils. The research was done using commercial software VADOSE/W in analyzing the changes in moisture content over a one-year period of time. Moisture content fluctuations from the numerical analyses were validated by the long-term moisture content measurements below the pavement of country road FM 2. The FM 2 model validation was done by comparing the numerical results of the moisture contents with those sensor measurements. Both numerical results and field measurements showed that moisture fluctuations tended to increase from the pavement center to the ditch center where negligible fluctuations were observed in the pavement center. The numerical results reached a good agreement with the measured moisture content fluctuations. The computed moisture content fluctuations in the expansive subgrade soils were employed for heave/shrinkage prediction of the subgrade soil based on the one-dimensional deformation assumption. The research achievements have shown that multiple weather conditions can be considered and integrated in commercial software VADOSE/W while predicting the moisture content fluctuations, which could lead to a more accurate heave/shrinkage prediction. This study is of great value in the sense that the research may help develop a proper

design and construction method to mitigate the harmful effect of expansive clays on highway pavements.

3.2 Site description of the FM 2 Project and the field investigation

Texas FM 2 is situated in Grimes County at the southeast side of Texas. Figure 11(a) shows FM 2 relative to other major big cities in Texas. The road consists of some total length 6.4 miles of which 2.4 miles is situated to the west of SH 6 (State Highway 6) at Courtney in Grimes County, TX and the other 4 miles continues towards east and ends at FM 365 as shown in Figure 11(b). The entire pavement was divided into 32 test sections, and moisture content sensors were installed at different stations. In this study, ECH_2O sensors were used to measure water content at different locations. These sensors are comparatively small, less expensive and required low power compared to other sensors (Zornberg et al. 2008). The measured moisture contents at stations 84, 99 and 184 were validated with the predicted results from the model.

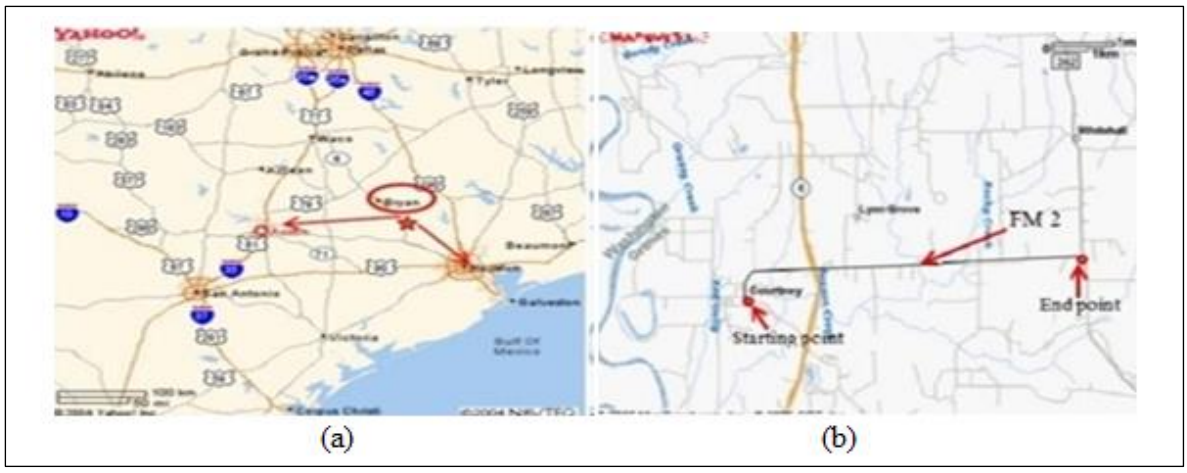

Figure 11. (a) Location of FM 2 relative to Austin and Houston (b) Layout of FM 2 (Zornberg et al., 2008).

For station 84 there were four horizontal sensors i.e. Nos. 31, 32, 33, and 34, as shown in Figure 12(a). They were located 152 mm below the pavement center line and continued to the right at a 2-m interval until the ditch was reached. Vertical sensors were installed at station 184 and 199 (below the ditch). Each of the two stations contained four sensors below the bottom of the ditch center vertically at the depths of 152 mm, 310 mm, 457 mm, and 610 mm, respectively. Figure 12 shows all the sensor locations.

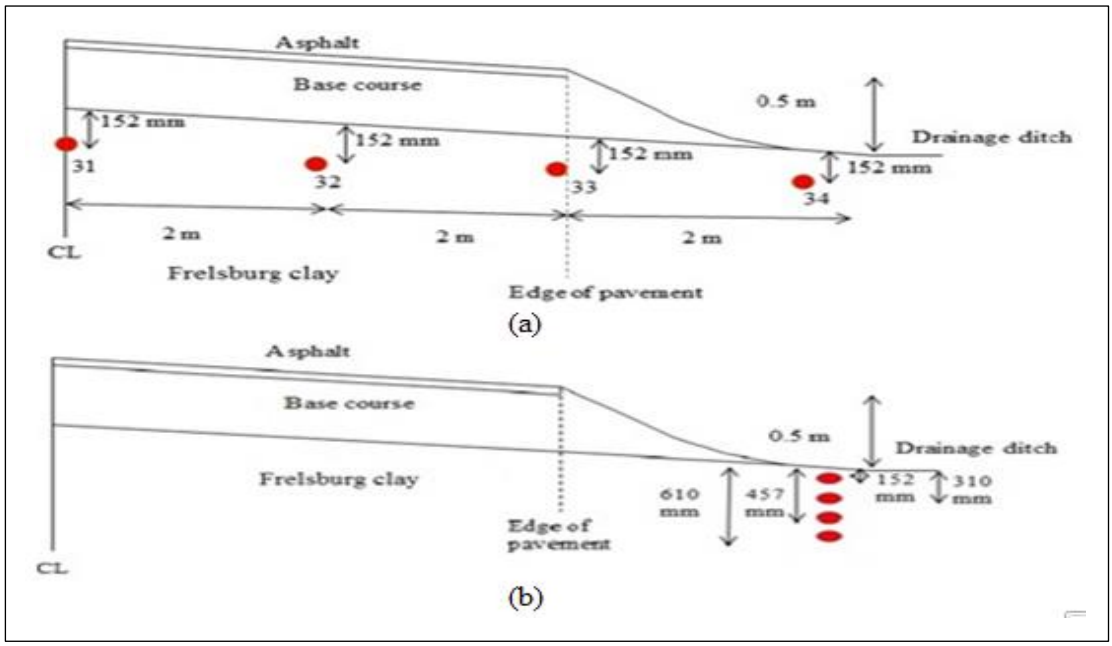

Figure 12. Sensor distributions: (a) Horizontal array at Station 84 (b) Vertical array at Stations 184 and 199 (Zornberg et al., 2008).

3.3 The VADOSE/W model setup

The soil profile presented in Figure 13 was modeled through the fully coupled transient analysis with VADOSE/W, a 2-D software package. The thickness of the soil profile was 2.7 m - a base of 0.5 m, followed by a subgrade of Frelsburg clay layer of 2.1 m, and a sand layer of 0.1 m. The thickness of the asphalt layer was 0.025 m (Gupta 2009). To collect surface runoff, drainage ditches were placed at two sides of the road, and each ditch was 0.5 m deep. The liquid limit (90) and plasticity index (65) of the Frelsburg clay (Soil Survey Staff, NRCS) clearly defined it as highly expansive clay. In this study, the pavement was used only as a soil cover, no structural loads were taken into consideration. Based on the availability of moisture sensor data, model simulation period was selected for a one -year period starting from February 2, 2006 and ending on February 1, 2007, as mentioned above.

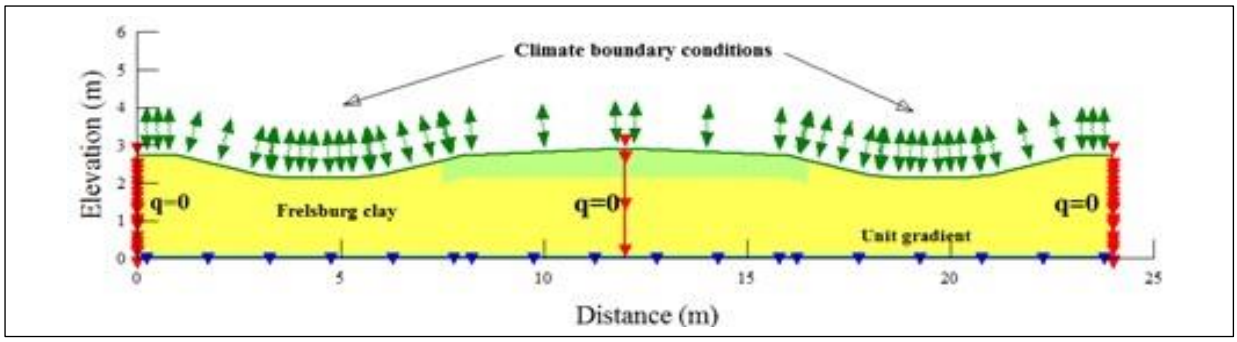

Figure 13. Soil profile with materials and boundary conditions.

The material properties that are required for a VADOSE/W hydrological model are the soil water characteristic curve (SWCC) and the hydraulic conductivity function (HCF). The SWCC defines the relationship between soil water content and suction, and the HCF presents the relationship between the hydraulic conductivity and the suction. The SWCC was generated through VADOSE/W by Fredlund and Xing (1994) equation. The saturated hydraulic conductivity of Frelsburg clay was used for creating the HCF graph. The soil water characteristic curve and hydraulic conductivity used for Frelsburg clay are shown below in Figure 14(a) and Figure 14(b), respectively.

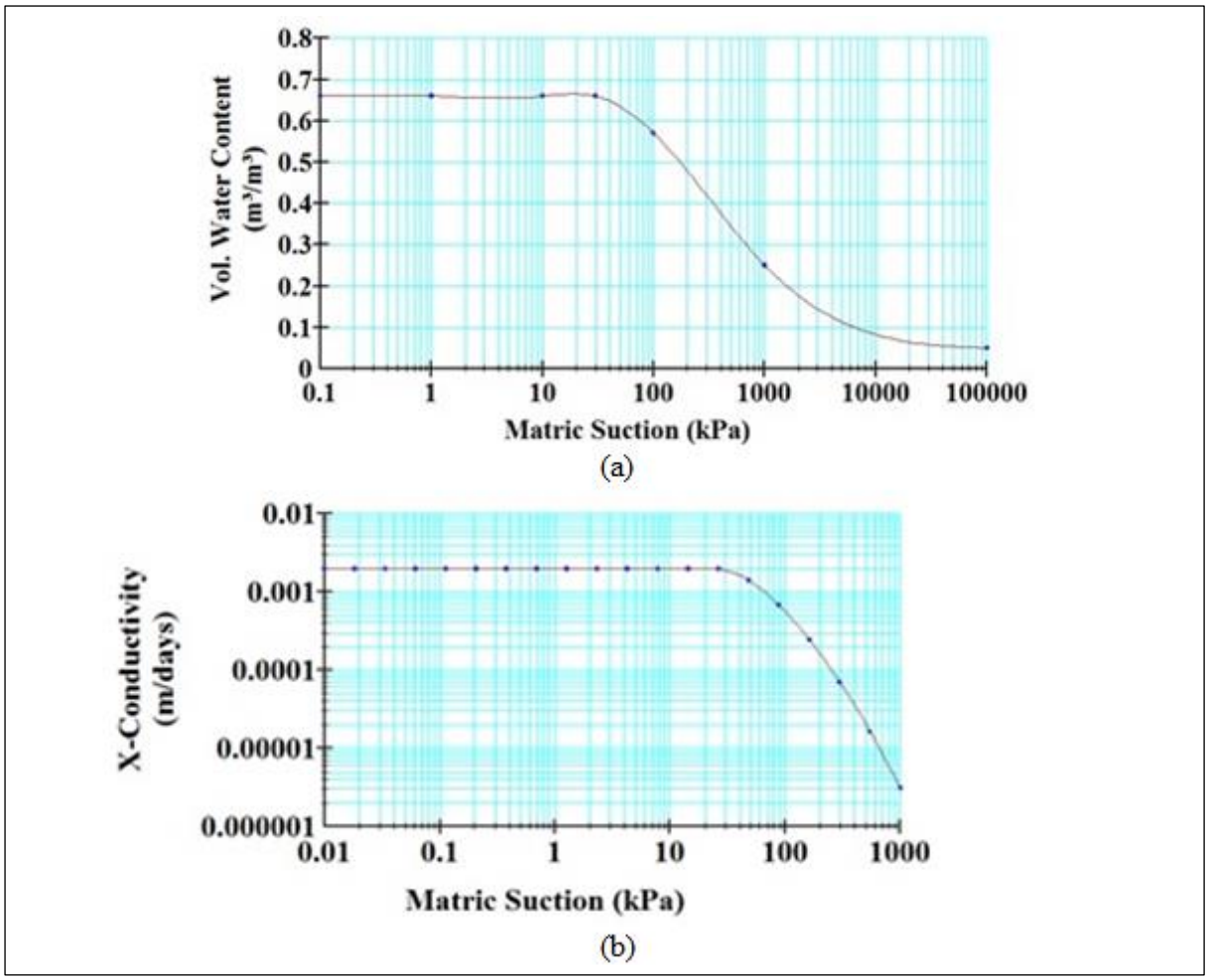

Figure 14. a) The SWCC used in VADOSE/W model, b) The HCF used in VADOSE/W model (Ikra 2017).

The initial conditions with the soil water content, soil matric suction, and soil temperature were generated by running a steady-state analysis using the same software package. The steady-state analysis was to generate the initial water content profile from the measured water content at specific positions on February 2, 2006. This process was completed by varying the pressure head for different layers until the estimated value of the initial water content matched with the measured ones at the specific positions. After the initial water content profile was created, the steady analysis outcomes were saved as a parent analysis file for the transient analysis.

Two types of boundary conditions were used in the transient analysis; the hydraulic boundary condition and climate boundary condition. The one-year daily weather data (February 2, 2006 - February 1, 2007) collected from College Station, Bryan District of Texas, were used to assign the climate boundary condition. A latitude of 30.680 degree was assigned for the study area to ensure the actual

evaporation estimation through VADOSE/W. Figures 15, 16, and 17 show the climate data used for the simulation. These data were collected as tabulated form from online sources of NOAA and represented as graphs here.

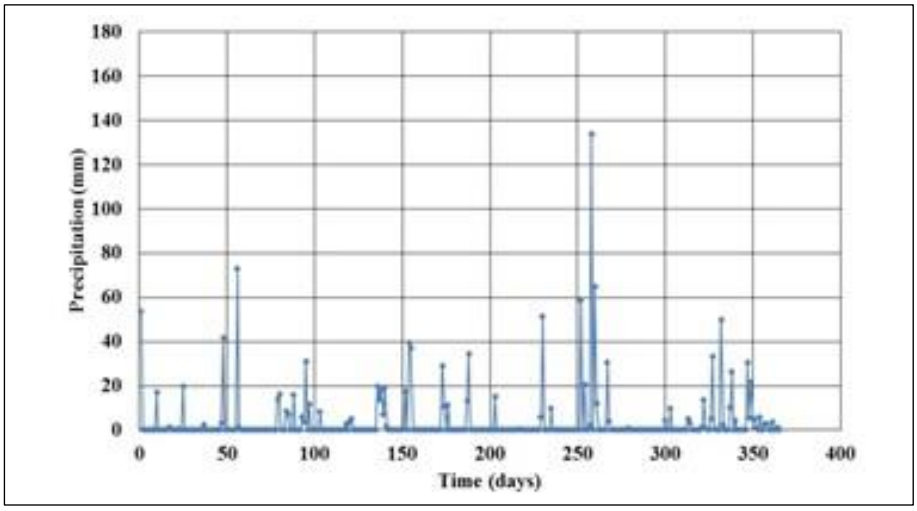

Figure 15. Precipitation data over a one-year duration.

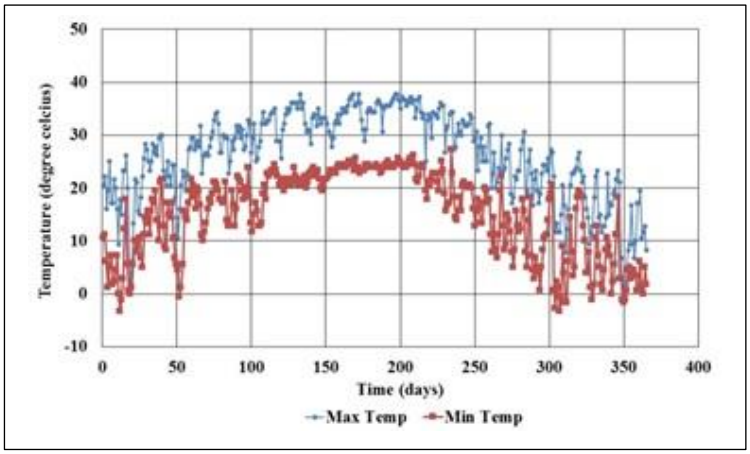

Figure 16. Temperature data (maximum and minimum) over a one-year duration.

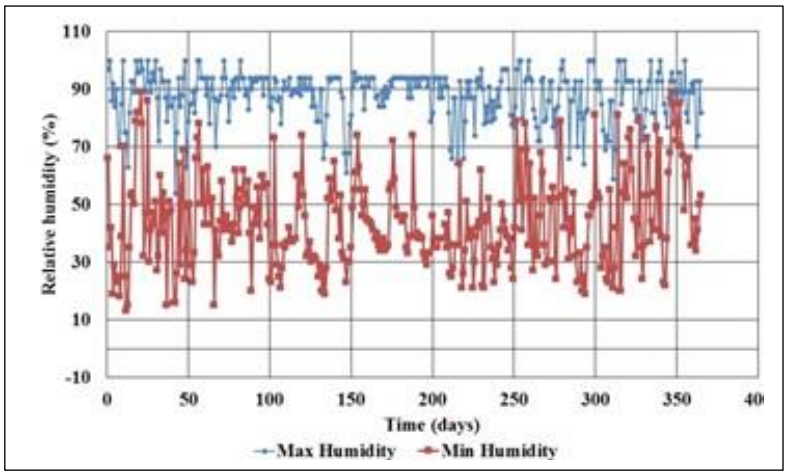

Figure 17. Relative humidity data (maximum and minimum) over a one-year duration.

A “no flow” (q=0) hydraulic boundary condition was applied at two sides of the model domain. Because of the symmetry, centerline of the pavement was also considered as no flow condition. The unit gradient was applied as the bottom boundary condition of the model as shown in Figure 3 to ensure free drainage. In VADOSE/W, unit gradient can be applied at the bottom of the model domain when the entire profile is not modeled.

3.4 Numerical validation with the field investigation

The validation was done for three individual stations (stations 84, 184 and 199). Results are presented and discussed as follows.

3.4.1 Station 184

At station 184, the measured water contents at this location varied between 26% and 43% where the simulated results varied in a range from 26% to 43%. Figure 18 shows the isochrones of gravimetric water content data below the ditch for station 184, with measured water content presented in Figure 18(a) and calculated water content shown in Figure 18(b).

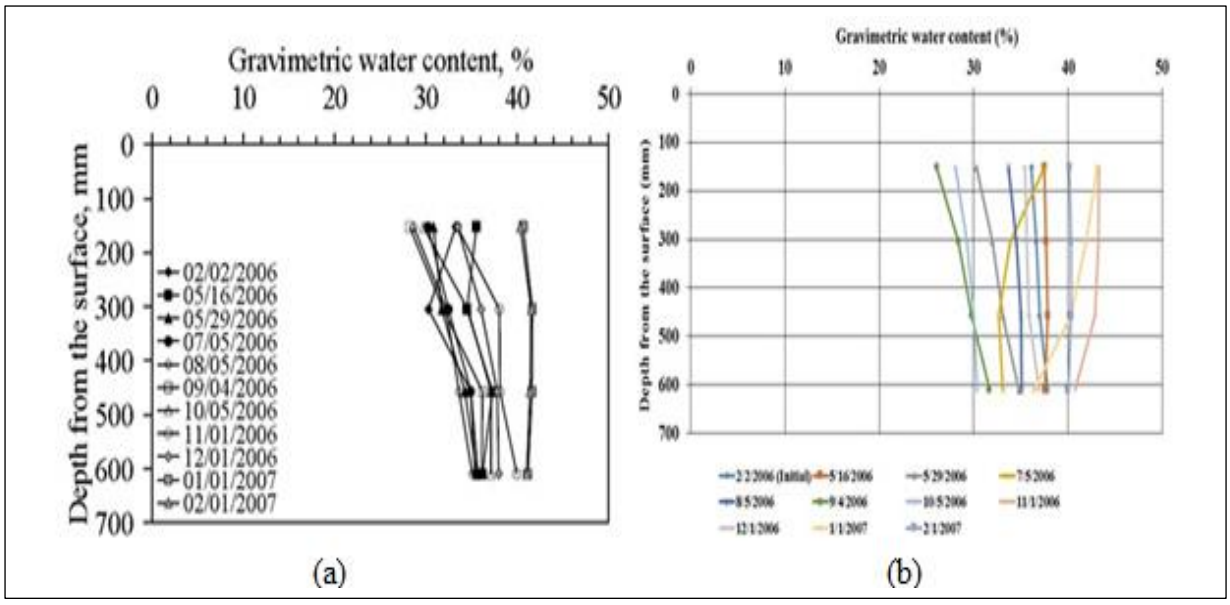

Figure 18. (a) Isochrones of measured gravimetric water content data for station 184 (Gupta, 2009), (b) Isochrones of simulated gravimetric water content data for station 184.

Figure 19 (b) shows the numerical results of gravimetric water content from February 2006 to February 2007. It was observed that the fluctuation of moisture content was 20%-43% for the period of one year (Figure 19 (b)), which is close to the measured data (27%-45%) shown in Figure 19 (a).

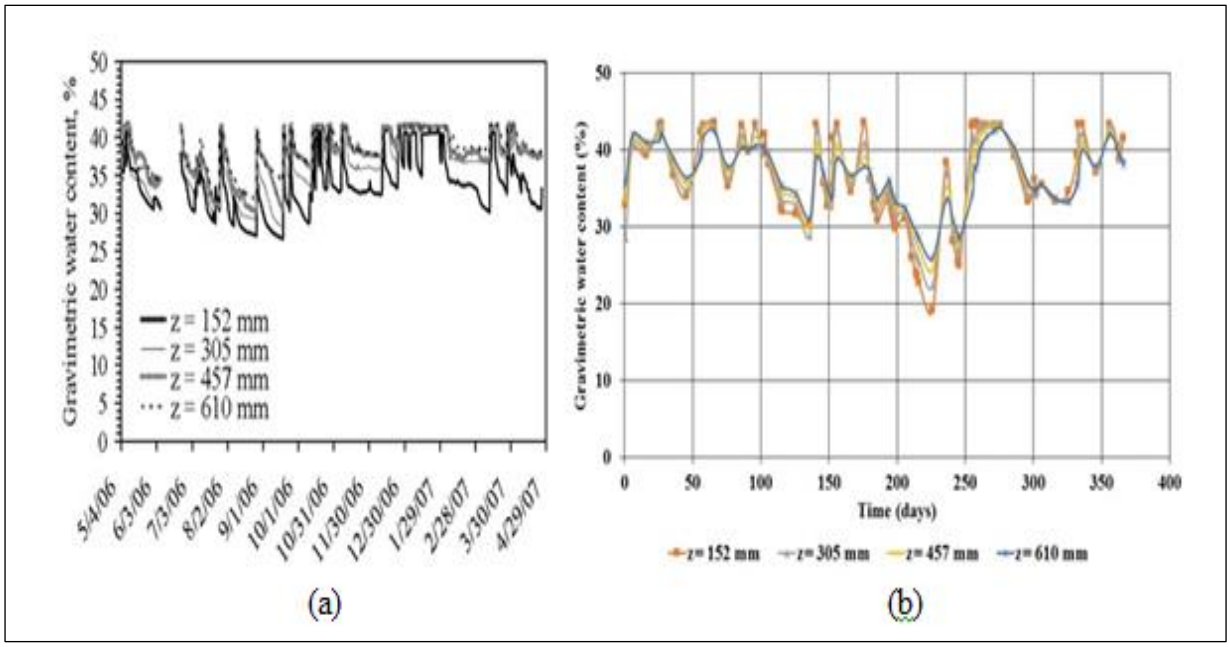

Figure 19. (a) Time series of measured gravimetric water content data below the ditch for Station 184 (Gupta, 2009), (b) Time series of simulated gravimetric water content data below the ditch for Station 184.

3.4.2 Station 199

A vertical array of sensors were installed in the drainage ditch at station 199. This station also showed the moisture movement through the subgrade soil. This location was shaded by trees, which explained why the moisture content in the subgrade below the drainage ditch did not reach its lowest level as compared with that at station 184. The measured water contents at this location varied between 33% and 43% whereas the simulated results varied from 26% to 43%. Figure 20 shows the isochrones of gravimetric water content data for station 199. Additionally, Figure 21 shows the time series of gravimetric water content for station 199.

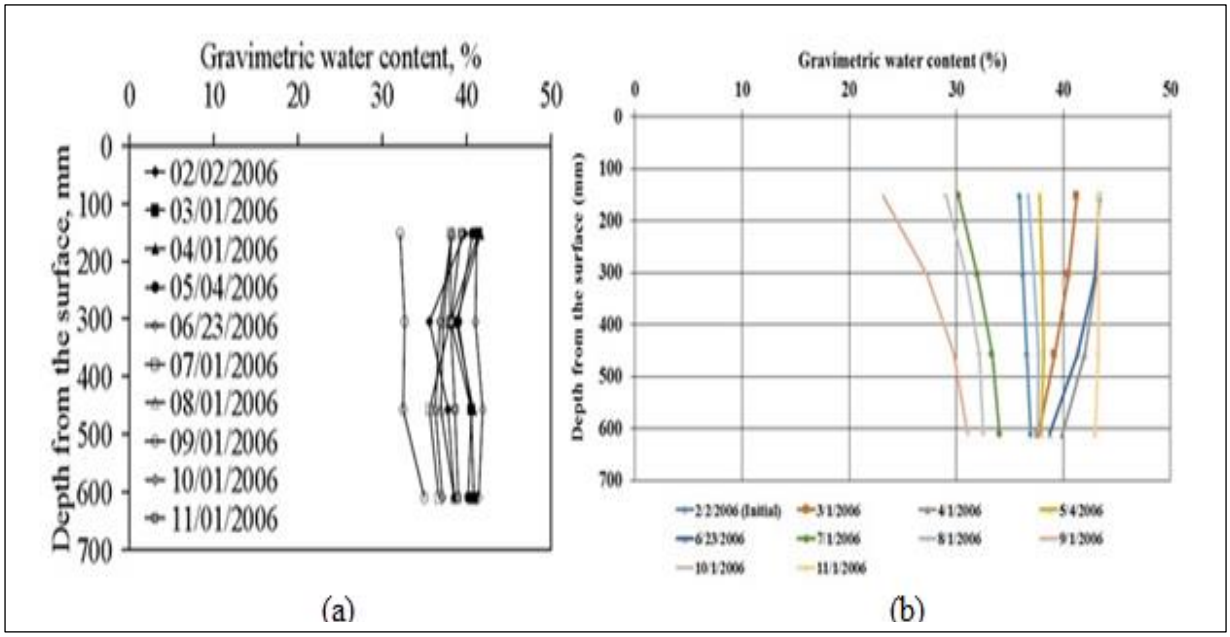

Figure 20. (a) Isochrones of measured gravimetric water content data below ditch (Station 199) (Gupta, 2009), (b) Isochrones of simulated gravimetric water content data below ditch (Station 199).

Figure 21 (b) shows the numerical results of gravimetric water content from February 2006 to February 2007. It has been observed that the fluctuation of moisture content was between 5% and 43% for the period of time, which is not close to the measured data (30%-45%). This section showed more fluctuation in the numerical analysis results. It is primarily because in the field, this section was reinforced by geosynthetics. But in numerical simulation, no reinforcement was considered. Besides, the tree effects specifically in this area were discarded in the simulation.

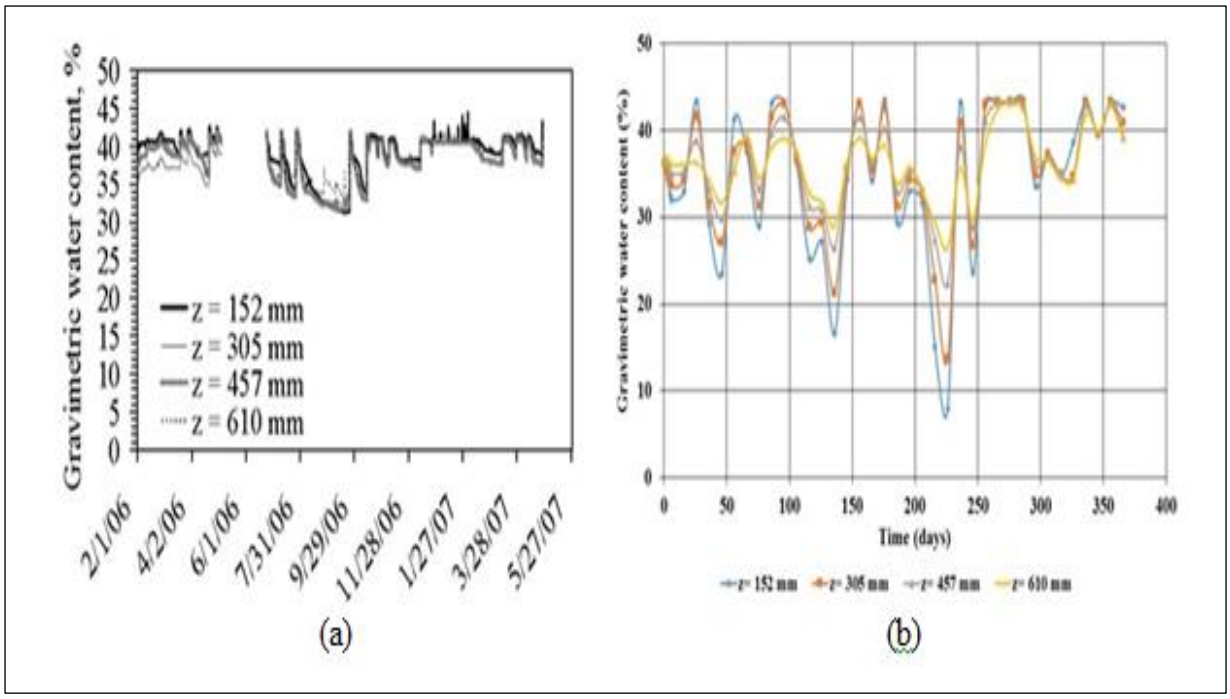

Figure 21. (a) Time series of measured gravimetric water content data below ditch (Station 199) (Gupta, 2009), (b) Time series of simulated gravimetric water content data below ditch (Station 199).

3.4.3 Station 84

At station 84, horizontal moisture sensor arrays were also installed below pavement for monitoring water content change. Figure 22 (a) shows the measured isochrones of gravimetric water content data for station 84 and Figure 22 (b) shows the simulated water contents at the same period of time when field measured moisture contents were taken. The simulation results showed more fluctuations at the pavement edge than the measured moisture content. Because in the field this station was stabilized with lime, but lime treatment was not reflected through VADOSE/W.

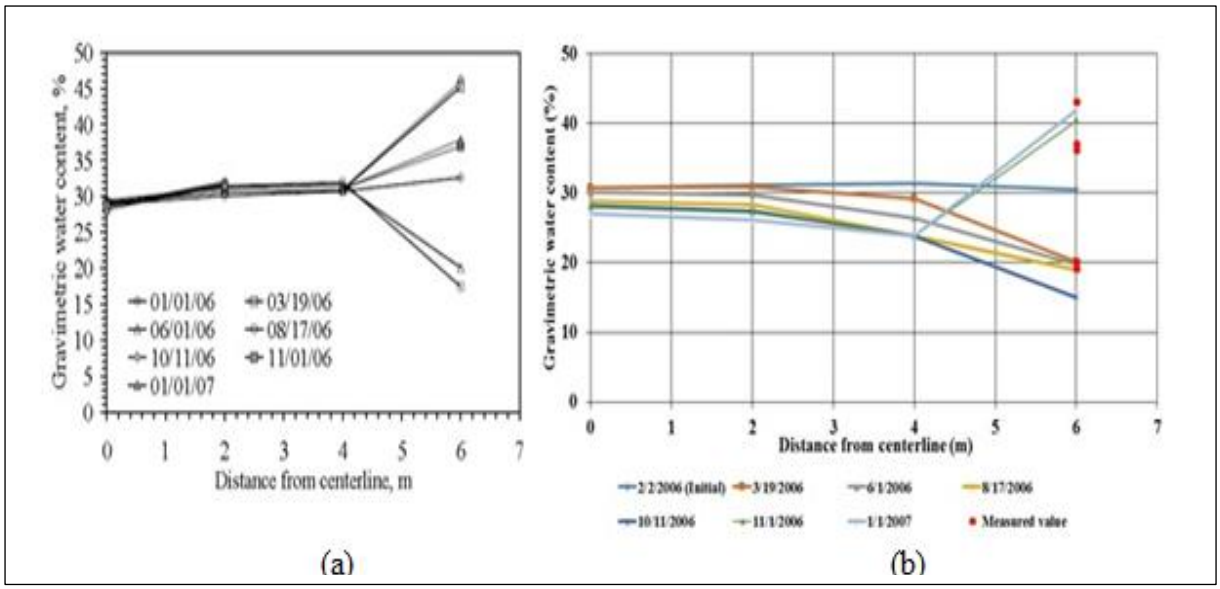

Figure 22. (a) Isochrones of measured gravimetric water content data for Station 84 - (Gupta 2009), (b) Isochrones of simulated gravimetric water content data for Station 84.

In Figure 23 the time series of the measured values indicates that sensor 31, 32, or 33 shows less fluctuation as they were situated below the pavement but sensor 34 demonstrated significant fluctuations because it laid below the ditch. In the case of simulation, there were insignificant fluctuations at the locations of sensors 31 and 32. However more fluctuations were found at the location of sensor of 33 than expected. Since this sensor was located near the ditch, it showed some more fluctuations. Expected fluctuations happened at the location of sensor 34.

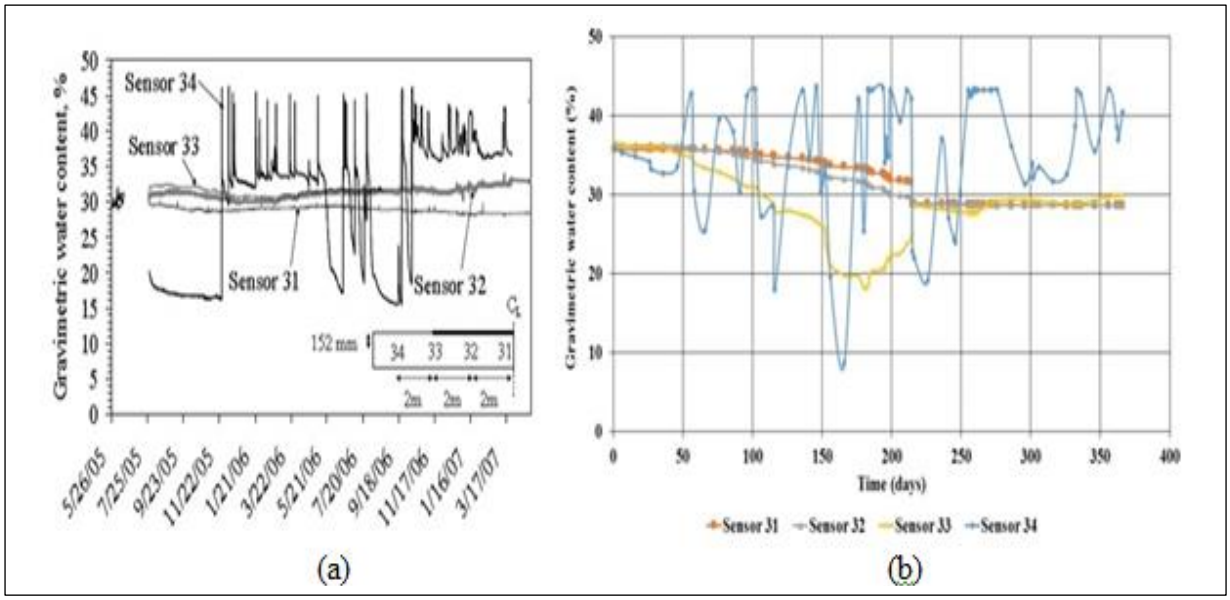

Figure 23. (a) Time series of measured gravimetric water content data below pavement (Station 84) (Gupta, 2009), (b) Time series of simulated gravimetric water content data below pavement (Station 84).

3.5 Heave/Shrinkage-induced deformation of the subgrade soil

After the water content and its distribution in the expansive subgrade layer were predicted, the vertical deformation induced from the heave or shrinkage could be estimated following an empirical equation. For the analyses, two extreme weather conditions were taken into consideration: the driest and the wettest. In the study period, precipitation occurred only 80 days throughout the year and temperature was high. So, shrinkage of the subgrade was expected.

Three sections were selected for deformation analysis: Section 1 was located below the pavement center, section 2 below the pavement edge and section 3 below the ditch. In this research, a subgrade depth of 2,100 mm was used for the calculations of heave/shrinkage-induced deformation. The total depth was divided into seven layers with a thickness of 300 mm for each layer for sections 1 and 2, respectively. For section 3 the expansive soil stratum was divided into eight sub-layers with a thickness of 78 mm for the first sub-layer, 152 mm each for the subsequent four sub-layers, and 500 mm each for the last three sub-layers of. The subgrade was divided this way to make the measured water contents conveniently utilized in the deformation calculations. The sections considered for the deformation analyses are shown in Figure 24.

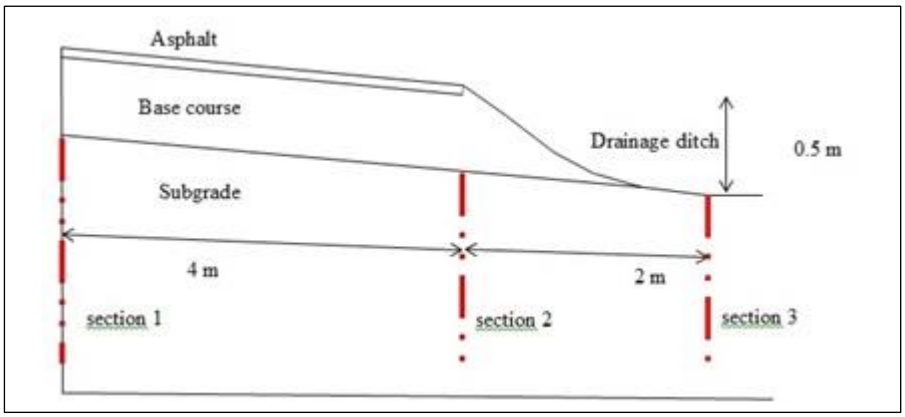

Figure 24. Sections for heave analysis.

Moisture content fluctuations used for the prediction of heave/shrinkage-induced deformation below the three pavement sections are shown in Figure 25.

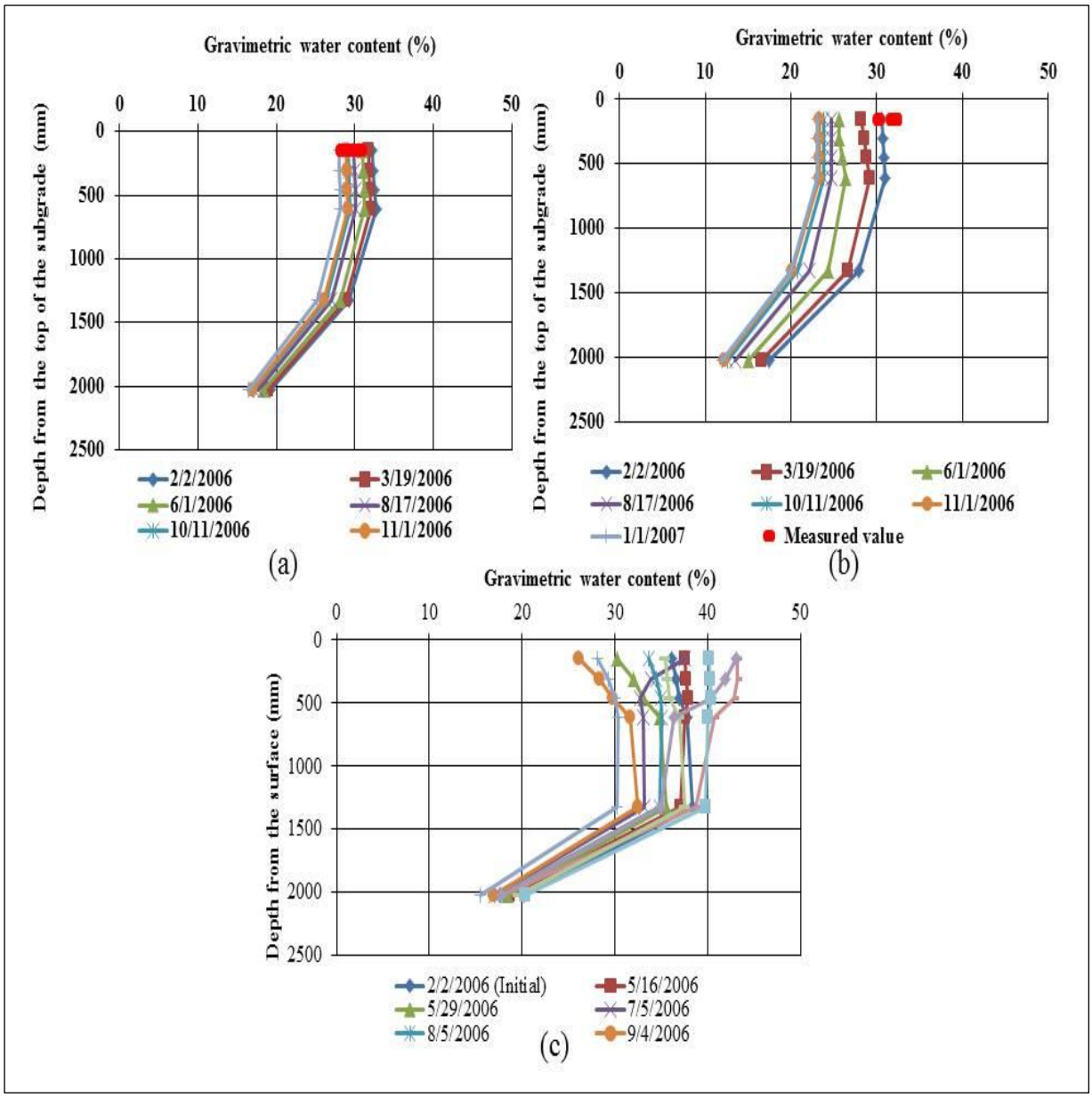

Figure 25. Moisture fluctuations with depth (a) section 1 (below pavement center), (b) section 2 (pavement edge) and (c) section 3 (ditch center).

Heave/shrinkage-induced deformation was calculated with the Richard (1967) and Dhowian (1990) equations. For the Dhowian equation the soil compressibility index α in equation 43 was assumed 0.33 and the specific gravity G_s was taken as 2.7 (Zornberg et al., 2008) The initial void ratio e_0 was taken as 0.75, which was obtained from the assumed initial porosity n=0.43 (Zornberg et al., 2008). For the numerical simulation, the initial void e_0 was calculated using equation $e = \frac{wG_s}{S}$. Here, the degree of saturation *S* and water content *w* were taken from the outcome of VADOSE/W. Following the tradition, sign (-) denotes the downward soil shrinkage.

Table 4 below shows the shrinkage-induced deformation for section 1. The bold line showed the comparison between deformation results from both measured and calculated water contents for the first sub-layer.

At section 1, sub-layer 1 had both the measured and simulated water content. The rest of the sub-layers calculated the water content only. For sub-layer 1, the shrinkage deformation corresponding to the measured and calculated water content from the both formulas (i.e. Richard and Dhowian equations) showed a good agreement. For other sub-layers both formulas gave good approximations as well. It can be seen that section 1 at the pavement center experienced a minimum amount of deformation as expected since water content change below the pavement center was insignificant. Table 5 shows the shrinkage calculations for section 2.

Table 4 Shrinkage deformation calculation for section 1 from the measured and calculated water content using the Richard and Dhowian equations, respectively.

No. of sub-layers	**Thickness (mm)**	**Change in water content (%)($w_{dry} - w_{initial}$)**	**Change in water content (%)($w_{dry} - w_{initial}$)**	**Richards formula (Shrinkage), mm**	**Richards formula (Shrinkage), mm**	**Dhowian formula (Shrinkage), mm**	**Dhowian formula (Shrinkage), mm**
		Measured	Calculated	From measured water content	Calculated	From measured water content	Calculated
1	**300**	**-1.5**	-3.84	**-2.27**	**-5.34**	**-1.77**	**-4.78**
2	300		-3.87		-5.37		-4.83
3	300		-3.89		-5.40		-4.89
4	300		-3.92		-5.44		-4.91
5	300		-3.67		-5.32		-4.77
6	300		-2.60		-4.40		-3.90
7	300		-3.18		-5.66		-5.00
pavement heave/ shrinkage deformation at the top of the ground surface, mm					-36.93		-33.08

Table 5 Shrinkage deformation calculation for section 2 from the measured and calculated water content using the Richard and Dhowian equations, respectively.

No. of sub-layers	**Thickness (mm)**	**Change in water content (%)($w_{dry} - w_{initial}$)**	**Change in water content (%)($w_{dry} - w_{initial}$)**	**Richards formula (Shrinkage deformation), mm**	**Richards formula (Shrinkage deformation), mm**	**Dhowian formula (Shrinkage deformation), mm**	**Dhowian formula (Shrinkage deformation), mm**
		Measured	Calculated	Measured	Calculated	Measured	Calculated
1	**300**	**-3**	**-7.95**	**-4.41**	**-11.68**	**-4.58**	**-10.64**
2	300		-7.82		-11.52		-10.55
3	300		-7.70		-11.36		-10.53
4	300		-7.58		-11.21		-10.33
5	300		-7.92		-12.21		-10.98
6	300		-5.40		-9.92		-9.05
7	300		-5.47		-10.10		-8.81
Surface heave/shrinkage (at top of the ground surface), mm					-78.02		-70.92

Table 6 Shrinkage deformation calculation for measured and calculated water content change from the Richard and Dhowian equations for section 3.

No. of sub-layers	**Thickness (mm)**	**Change in water content (%) ($w_{dry} - w_{initial}$)**	**Change in water content (%) ($w_{dry} - w_{initial}$)**	**Richards formula (Shrinkage), mm**	**Richards formula (Shrinkage), mm**	**Dhowian formula (Shrinkage), mm**	**Dhowian formula (Shrinkage), mm**
		Measured	Calculated	Measured	Calculated	Measured	Calculated
1	**78**	**-11**	**-8**	**-4.20**	**-3.25**	**-4.37**	**-2.93**
2	**152**	**-6**	**-9.4**	**-5.92**	**-6.57**	**-4.64**	**-5.91**
3	**152**	**1**	**-9.7**	**-3.17**	**-6.58**	**0.77**	**-5.94**
4	**152**	**1**	**-7**	**-6.00**	**-4.79**	**0.77**	**-4.36**
5	**152**	**-1**	**-5.5**	**-4.70**	**-3.74**	**-0.77**	**-3.42**
6	500		-5		-11.11		-10.22
7	500		-6		-13.88		10.72
8	500		-6		-16.38		0.78
Surface heave/shrinkage (at top of the ground surface), mm					-66.30		-59.43

Table 7 Heave deformation calculation for measured and calculated water content change from the Richard and Dhowian equations for section 3.

No. of sub-layers	**Thickness (mm)**	**Change in water content (%) ($w_{wet} - w_{initial}$)**	**Change in water content (%) ($w_{wet} - w_{initial}$)**	**Richards formula (Heave), mm**	**Richards formula (Heave), mm**	**Dhowian formula (Heave), mm**	**Dhowian formula (Heave), mm**
		Measured	Calculated	Measured	Calculated	Measured	Calculated
1	**78**	**23**	**23.5**	**10.48**	**10.90**	**9.13**	**8.60**
2	**152**	**17**	**17**	**7.45**	**13.66**	**13.16**	**10.61**
3	**152**	**13**	**15.2**	**8.25**	**11.84**	**10.06**	**9.52**
4	**152**	**8**	**13**	**9.07**	**9.83**	**6.19**	**8.10**
5	**152**	**12**	**8.7**	**7.02**	**6.38**	**9.29**	**5.40**
6	500		7		16.66		14.15
7	500		6		15.14		12.62
8	500		7		21.20		17.84
Surface heave/shrinkage deformation (at top of the ground surface), mm					105.62		86.83

For section 2, sub-layer 1 had both the measured and simulated water content. The rest of the sub-layers had calculated water content only. For sub-layer 1, shrinkage deformation for measured and simulated water content from both of the Richard and Dhowian formulas were comparable. For other sub-layers both formulas also gave good approximations. Tables 6 and 7above showed the shrinkage and heave deformations for section 3, respectively.

For section 3, the first five sub-layers had both the measured and simulated water content. The rest of the three layers had simulated data only. For the first five sub-layers, heave/shrinkage deformation from the measured and simulated water content was overall reasonably close based on the Richard and Dhowian formulas, respectively. For the other sub-layers, both formulas also gave acceptable approximations. It is observed that heave/shrinkage deformation occurred primarily in the unpaved portion of the pavement, i.e. in the ditch part because it had a direct response to weather change. No heave deformation occurred to the subgrade soils between the pavement center and edge because the water content gradually decreased from the beginning of the one-year duration. Based on the analyses, it

can be seen that maximum shrinkage deformation occurred at the pavement edge. Due to high temperature and lack of precipitation water content started decreasing from the beginning of the one-year duration. After the month of October, when rainfall started on a regular basis with decreasing temperature, water content increased gradually. As the ditch had a direct interaction with precipitation and temperature, after a certain amount of time the water content below the ditch increased and crossed the initial water content line. In case of the pavement center water content could not increase with time because the impermeable pavement did not allow the rain to infiltrate. Therefore, the water content kept decreasing and it caused shrinkage.

The pavement edge had a little more interaction with weather change than the pavement center. Usually, Pavement crack starts from pavement edge and gradually travels to the pavement center (Zornberg et al. 2008). Based on the filed observation, the amount of heave/shrinkage deformation was not risky for the generation of pavement crack. However, the simulation and measurement were done for one year only, and an entire picture of water content fluctuation were not able to be achieved. Generally in engineering practice, the repeating heave/shrinkage may cause longitudinal cracks on the pavement. If there were any water infiltration source (leakage) in the paved portion, it would cause a drastic change in water content in the subgrade soils. These huge water content changes may cause severe heave to the pavement sections.

4. Summary

The geosynthetic-reinforced pavement, subjected to the heave/shrinkage-induced vertical displacement caused by the volume change of expansive subgrade soils, was formulated by following the Timoshenko beam theory. The virtual load method (VLM) was developed by applying a virtual load on the pavement to make the beam deflection equivalent to the heave/shrinkage-induced vertical displacement. The unknown virtual load was expressed as a Fourier series, and the Fourier constants were determined by employing the inverse theory for the identification of material parameters. A rigorous analytical solution for evaluating the shear force, bending moment etc. acting on geosynthetic reinforced pavement resting over expansive soil was developed.

A case study has been carried out to investigate the performance of the pavement of country road FM 2 in Texas overlying on expansive subgrade soils. The effects of shear stiffness and tension modulus of elasticity of the geosynthetics (geogrid or geotextile) have been studied for the pavement sections, which were reinforced with geosynthetics for the extreme heave and shrinkage conditions, respectively. Results have shown that the methodology was successfully applied to analyze the real engineering case. It can be used as a simple and reliable method for pavement design. Geosynthetics without shear stiffness (e.g. geotextile) resist less shear force or bending moment than geosynthetics with shear stiffness (e.g. geogrid) do. The analysis of tension force variations due to the changes in tension modulus can assist pavement designers and industry to select size and type of geosynthetics to reinforce pavements overlying expansive subgrade soils to reduce the damages caused by seasonal swelling and shrinkage of the expansive soils.

A numerical model was established to analyze moisture content fluctuations in the subgrade expansive soils below the pavement of country road FM 2 near the city of College Station in Texas, USA. The numerical simulations were completed through commercial software package VADOSE/W. The focus of this research was to predict the vertical movement of unsaturated expansive soils with the effect of climate change. In this research, field-measured moisture contents were compared with those numerical results, and it turned out that the numerical moisture contents

at the specific locations were comparable with the measurements. In the field four vertical sensors were installed below each ditch (two ditches @ station 184 and station 199 respectively) and four horizontal sensors were installed below the pavement at station 84. At station 184 the measured water contents varied between 26% and 43% and the simulated water contents varied in the same range between 26% and 43%, whereas at station 199 the measured water contents were in the range from 33% to 43%, and the simulated water contents varied from 26% to 43%. At station 84, the measured water contents below the pavement from center to edge varied from 28% to 30% and the simulated water content varied between 26% and 43%, but the measured water contents below the ditch differed from 16% to 43% and the simulated water contents varied from 19% to 43%. This validated model was used for analyzing moisture content change in the subgrade expansive soils at different pavement sections below pavement. Ground heave/shrinkage deformation was calculated following the Richard (1967) and Dhowian (1990) formulas, respectively for two extreme weather conditions at three different locations; the pavement center, the edge and the ditch center. The calculated maximum shrinkage deformation at ground surface for the pavement center, edge and ditch center were 36.93mm, 79 mm and 66.30 mm respectively, whereas the calculated maximum 105 mm heave deformation occurred at the top surface of the ditch center with no heave happened below the pavement. Due to continuous decreases in water content below the pavement, the subgrade expansive soil experienced no heave. But at the ditch center the expansive soil had both heave and shrinkage deformation for the two extreme conditions, respectively.

The effective prediction of the seasonal water content variations in the expansive subgrade soils indicated that Vadose/W could be a useful tool for pavement engineers to predict the heave/shrinkage deformation of the pavements on expansive soils. It has been proved that the successful establishment of the model was capable of providing reliable results of water content distribution below the ground surface.

5. References

Adem, H. H. (2015). *Modulus of Elasticity Based Method for Estimating the Vertical Movement of Natural Unsaturated Expansive Soils*, PhD. Dissertation, University of Ottawa, Ontario, Canada.

Adem, H. H., and Vanapalli, S. K. (2013). “Constitutive modeling approach for estimating 1-D heave with respect to time for expansive soils.” *International Journal of Geotechnical Engineering*, Taylor & Francis, 7(2), 199–204.

Al-Rawas, A. A., and Goosen, M. F. A. (2006). *Expansive Soils: Recent Advances in Characterization and Treatment*. CRC Press.

Alonso, E. E., Gens, A., and Josa, A. (1990). “A constitutive model for partially saturated soils.” *Géotechnique*, Citeseer, 40(3), 405–430.

Aster, R. C., Borchers, B., and Thurber, C. H. (2013). “Linear Regression.” *Parameter Estimation and Inverse Problems*, Elsevier, 25–53.

Booth, A. J. (2014). “Impacts of desiccation cracking and climate change on highway cutting hydrology, PhD. Dissertation.” Loughborough University, UK.

Briaud, J.-L., Zhang, X., and Moon, S. (2003). “Shrink test–water content method for shrink and swell predictions.” *Journal of geotechnical and geoenvironmental engineering*, American Society of Civil Engineers, 129(7), 590–600.

Cary, C. E., and Zapata, C. E. (2014). “Unsaturated Soil Modeling for Airfield Pavement Design.” *Journal of Transportation Engineering*, 140(1), 50–60.

Chen, F. H. (1988). *Foundations on Expansive Soils*. Elsevier, New York.

Chenggang, B. (2004). “Study on the interaction behavior of geosynthetics and soil in China.” *Ningbo Institute of Technology, Zhejiang University, China*.

Chittoori, S., Pedarla, A., Puppala, A. J., Hoyos, L. R., Nazarian, S., and Saride, S. (2011). “Leachate studies on lime and portland cement treated expansive clays.” *Geo-Frontiers 2011: Advances in Geotechnical Engineering*, 4479–4488.

Cowper, G. R. (1966). “The Shear Coefficient in Timoshenko’s Beam Theory.” *Journal of Applied Mechanics*, 33(2), 335.

Dang, L. C., Fatahi, B., and Khabbaz, H. (2016). “Behaviour of expansive soils stabilized with hydrated lime and bagasse fibres.” *Procedia engineering*,

Elsevier, 143, 658–665.

Das, R. (2012). “Inverse analysis of Navier–Stokes equations using simplex search method.” *Inverse Problems in Science and Engineering*, 20(4), 445–462.

Dhowian, A. W. (1990). “Simplified heave prediction model for expansive shale.” *Geotechnical Testing Journal*, ASTM International, 13(4), 323–333.

Djellali, A., Ounis, A., and Saghafi, B. (2013). “Behavior of Flexible Pavements on Expansive Soils.” *International Journal of Transportation Engineering*, Tarrahan Parseh Transportation Research Institute, 1(1), 1–16.

Estabragh, A. R., Rafatjo, H., and Javadi, A. A. (2014). “Treatment of an expansive soil by mechanical and chemical techniques.” *Geosynthetics International*, Thomas Telford Ltd, 21(3), 233–243.

Fredlund, D. G., and Xing, A. (1994). “Equations for the soil-water characteristic curve.” *Canadian geotechnical journal*, NRC Research Press, 31(4), 521–532.

Fwa, T. F., Shi, X. P., and Tan, S. A. (1996). “Use of Pasternak foundation model in concrete pavement analysis.” *Journal of transportation engineering*, American Society of Civil Engineers, 122(4), 323–328.

Geo-Slope. (2007). *Vadose Zone Modeling with VADOSE/W 2007: An Engineering Methodology*. Calgray, Alberta.

Ghosh, B., Fatahi, B., Khabbaz, H., and Yin, J.-H. (2017). “Analytical study for double-layer geosynthetic reinforced load transfer platform on column improved soft soil.” *Geotextiles and Geomembranes*, Elsevier, 45(5), 508–536.

Golub, G. (1965). “Numerical methods for solving linear least squares problems.” *Numerische Mathematik*, 7(3), 206–216.

Gupta, R. (2009). “A study of geosynthetic reinforced flexible pavement system, PhD. Dissertation.” University of Texas, Austin, TX.

Ikra, B. A. (2017). “Predictions of Moisture Content Changes and Heave Analyses of Expansive Soils Under Extreme Weather.” M. S. Thesis, Louisisana Tech University, Ruston, LA, USA.

Jahandari, S., Li, J., Saberian, M., and Shahsavarigoughari, M. (2017). “Experimental study of the effects of geogrids on elasticity modulus, brittleness, strength, and stress-strain behavior of lime stabilized kaolinitic clay.” *GeoResJ*,

Elsevier, 13, 49–58.

Khan, A. (2017). “Influence of Moisture Content Distribution in Soil on Pavement and Geothermal Energy.” Ph.D. Dissertation, Louisiana Tech University, Ruston, LA, USA.

Khan, M. A., and Wang, J. W. (2017). “Application of Euler-Bernoulli Beam on Winkler Foundation for Highway Pavement on Expansive Soils.” *Proc., PanAm-UNSAT 2017: Second Pan-American Conference on Unsaturated Soils, ASCE. (Accepted)*.

Kumar, A., Walia, B. S., and Bajaj, A. (2007). “Influence of fly ash, lime, and polyester fibers on compaction and strength properties of expansive soil.” *Journal of materials in civil engineering*, American Society of Civil Engineers, 19(3), 242–248.

Levenberg, K. (1944). “A method for the solution of certain non-linear problems in least squares.” *Quarterly of Applied Mathematics*, 2(2), 164–168.

Luo, R., and Prozzi, J. A. (2010). “Development of longitudinal cracks on pavement over shrinking expansive subgrade.” *Road Materials and Pavement Design*, Taylor & Francis, 11(4), 807–832.

Ma, X., Butterworth, J. W., and Clifton, G. C. (2009). “Static analysis of an infinite beam resting on a tensionless Pasternak foundation.” *European Journal of Mechanics - A/Solids*, 28(4), 697–703.

Marquardt, D. W. (1963). “An Algorithm for Least-Squares Estimation of Nonlinear Parameters.” *Journal of the Society for Industrial and Applied Mathematics*, 11(2), 431–441.

Marquardt, D. W. (1970). “Generalized Inverses, Ridge Regression, Biased Linear Estimation, and Nonlinear Estimation.” *Technometrics*, 12(3), 591.

Marr, S. A., Gilbert, R. B., and Rauch, A. F. (2004). “A practical method for predicting expansive soil behavior.” *Geotechnical Engineering for Transportation Projects*, 1144–1152.

Moghal, A. A. B., Chittoori, B. C. S., Basha, B. M., and Al-Mahbashi, A. M. (2017). “Effect of polypropylene fibre reinforcement on the consolidation, swell and shrinkage behaviour of lime-blended expansive soil.” *International Journal of*

Geotechnical Engineering, Taylor & Francis, 1–10.

Musa, A. E. S. (2018). “An Analytical Bending Solution for Analysis and Design of Long Beams Constructed on the Expansive Soil.” *Arabian Journal for Science and Engineering*, Springer, 1–12.

Nelson, J. D., Chao, K.-C., and Overton, D. D. (2007). “Definition of expansion potential for expansive soil.” *Proceedings of the Third Asian Conference on Unsaturated Soils*.

Overton, D. D., Chao, K.-C., and Nelson, J. D. (2006). “Time rate of heave prediction for expansive soils.” *GeoCongress 2006: Geotechnical Engineering in the Information Technology Age*, 1–6.

Puppala, A. J., and Cerato, A. (2009). “Heave distress problems in chemically-treated sulfate-laden materials.” *Geo-Strata—Geo Institute of ASCE*, 28–30.

Richards, B. (1967). “Moisture flow and equilibria in unsaturated soils for shallow foundations.” *Permeability and Capillarity of Soils*, ASTM International.

Selvadurai, A. P. S. (1979). *Elastic Analysis of Soil-Foundation Interaction: Development in Geotechnical Engineering*. Elsevier, Amsterdam.

Siekmeier, J. (2011). “Implementation of Unsaturated Soil Mechanics During Pavement Construction QA.” *Geo-Strata—Geo Institute of ASCE*, ASCE, 15(1).

Stephen, N. G. (1980). “Timoshenko’s shear coefficient from a beam subjected to gravity loading.” *Journal of Applied Mechanics*, American Society of Mechanical Engineers, 47(1), 121–127.

Tanahashi, H. (2004). “Formulas for an infinitely long Bernoulli-Euler beam on the Pasternak model.” *Soils and foundations*, The Japanese Geotechnical Society, 44(5), 109–118.

Terzaghi, K. (1955). “Evaluation of Coefficient of Subgrade Reaction.” *Geotechnique, London*, 5(4), 41–50.

Timoshenko, S. P. (1921). “LXVI. On the correction for shear of the differential equation for transverse vibrations of prismatic bars.” *The London, Edinburgh, and Dublin Philosophical Magazine and Journal of Science*, Taylor & Francis, 41(245), 744–746.

Vesic, B. (1961). “Beams on Elastic Subgrade and the Winkler’s Hypothesis.” *Proc.*

5th International Conference on Soil Mechanics and Foundation Engineering, Paris, France, 845–850.

Vessely, M., and Wu, J. (2002). “Feasibility of geosynthetic inclusion for reducing swelling of expansive soils.” *Transportation Research Record: Journal of the Transportation Research Board*, Transportation Research Board of the National Academies, (1787), 42–52.

Viswanadham, B. V. S., Phanikumar, B. R., and Mukherjee, R. V. (2009). “Swelling behaviour of a geofiber-reinforced expansive soil.” *Geotextiles and Geomembranes*, Elsevier, 27(1), 73–76.

Vu, H. Q., and Fredlund, D. G. (2004). “The prediction of one-, two-, and three-dimensional heave in expansive soils.” *Canadian Geotechnical Journal*, NRC Research Press, 41(4), 713–737.

Vu, H. Q., and Fredlund, D. G. (2006). “Challenges to modelling heave in expansive soils.” *Canadian Geotechnical Journal*, NRC Research Press, 43(12), 1249–1272.

Worku, A. (2014). “Development of a calibrated Pasternak foundation model for practical use.” *International Journal of Geotechnical Engineering*, Taylor & Francis, 8(1), 26–33.

Wray, W. K., El-Garhy, B. M., and Youssef, A. A. (2005). “Three-dimensional model for moisture and volume changes prediction in expansive soils.” *Journal of Geotechnical and Geoenvironmental Engineering*, American Society of Civil Engineers, 131(3), 311–324.

Yin, J.-H. (2000a). “Comparative Modeling Study of Reinforced Beam on Elastic Foundation.” *Journal of Geotechnical and Geoenvironmental Engineering*, 126(3), 265–271.

Yin, J.-H. (2000b). “Closed-Form Solution for Reinforced Timoshenko Beam on Elastic Foundation.” *Journal of Engineering Mechanics*, 126(8), 868–874.

Yixian, W., Panpan, G., Shengbiao, S., Haiping, Y., and Binxiang, Y. (2016). “Study on strength influence mechanism of fiber-reinforced expansive soil using jute.” *Geotechnical and Geological Engineering*, Springer, 34(4), 1079–1088.

Yu, H., Cai, C., Yuan, Y., and Jia, M. (2017). “Analytical solutions for Euler-Bernoulli

Beam on Pasternak foundation subjected to arbitrary dynamic loads." *International Journal for Numerical and Analytical Methods in Geomechanics*, 41(8), 1125–1137.

Zapata, C., Perera, Y., and Houston, W. (2009). "Matric suction prediction model in new AASHTO mechanistic-empirical pavement design guide." *Transportation Research Record: Journal of the Transportation Research Board*, Transportation Research Board of the National Academies, (2101), 53–62.

Zhang, X. (2004). "Consolidation theories for saturated-unsaturated soils and numerical simulations of residential buildings on expansive soils, PhD. Dissertation." Texas A&M University, College Station, TX.

Zhao, L.-S., Zhou, W.-H., Fatahi, B., Li, X.-B., and Yuen, K.-V. (2016). "A dual beam model for geosynthetic-reinforced granular fill on an elastic foundation." *Applied Mathematical Modelling*, 40(21–22), 9254–9268.

Zornberg, J. G. (2017). "Functions and applications of geosynthetics in roadways." *Procedia engineering*, Elsevier, 189, 298–306.

Zornberg, J. G., Prozzi, J. A., Gupta, R., Luo, R., McCartney, J. S., Ferreira, J. Z., and Nogueira, C. (2008). *Validating Mechanisms in Geosynthetic Reinforced Pavements*. *Center for Transportation Research (CTR)*, Austin, Texas.